On the Evolution of Flows in Straight Circular Pipes subject to a Localized Transverse Impulsive Body Force

Giuseppe Di Labbio

A Thesis
in the Department of
Mechanical and Industrial Engineering

Presented in partial fulfillment
of the requirements for the degree
Master of Applied Science (Mechanical Engineering)
Concordia University
Montreal, Quebec, Canada

June 2015

CONCORDIA UNIVERSITY

School of Graduate Studies

This is to certify that the thesis prepared,

By: **Giuseppe Di Labbio**

Entitled: **"On the Evolution of Flows in Straight Circular Pipes subject to a Localized Transverse Impulsive Body Force"**

and submitted in partial fulfillment of the requirements for the degree of

Master of Applied Science (Mechanical Engineering)

Complies with the regulations of the University and meets the accepted standards with respect to originality and quality.

Signed by the Final Examining Committee:

_____ Chair
Dr. Onur Kuzgunkaya

_____ Examiner
Dr. Hoi Dick Ng

_____ Examiner
Dr. Nizar Bouguila — CIISE External

_____ Supervisor
Dr. Lyes Kadem

Approved by: _____
Dr. Sivakumar Narayanswamy, MASc Program Director
Department of Mechanical and Industrial Engineering

_____
Dean Amir Asif
Faculty of Engineering and Computer Science

Date:_____

Abstract

On the Evolution of Flows in Straight Circular Pipes subject to a Localized Transverse Impulsive Body Force

Giuseppe Di Labbio

In blunt traumatic aortic injury, it is highly debated whether an abrupt deceleration alone is sufficient to cause aortic rupture. Motivated by this debate, this fundamental study investigates the effects of a localized transverse impulsive body force acting on a straight circular pipe through numerical simulation for both constant and pulsatile inlet velocity profiles. Application of this impulsive force results in a transverse pressure gradient which skews counterclockwise with flow acceleration. This pressure gradient induces two counter-rotating streamwise vortices at the boundaries of the forced section with secondary flows developing in conjunction which act to restore the unforced velocity profile. The development of the secondary flow was observed to occur later for an accelerating flow and earlier for a decelerating flow. A dimensionless parameter, Ψ, was developed to characterize flows based on the ratio of transverse to streamwise pressure gradients. Lower Reynolds number flows (higher Ψ), were observed to be most readily affected by the body force. Maximum skewing of the velocity profile occurred during the impact rather than at the end except for a decelerating flow, with larger skewing occurring for higher Ψ. The temporal decay of kinetic energy was observed to be faster for larger Reynolds numbers and is governed by a power law decay. An alternating exchange in energy between the axial and secondary flows was also observed.

Acknowledgments

I owe my deepest and sincere gratitude to my supervisor, Dr. Lyes Kadem, for continuously supporting me, challenging me, and believing in me. Your guidance has been invaluable to me throughout my research and career thus far. It gives me great pleasure to work by your side and I look forward to working with you in the coming years. Thank you very much.

In addition, I am very grateful to the group in the Laboratory of Cardiovascular Fluid Dynamics for their technical and motivational support: Hani Abulkhair, Alexandre Bélanger, Emilia Benevento, Dr. Zahra Keshavarz-Motamed, and Azadeh Saeedi. I owe special thanks to Dr. Zahra for all her help and advice in my life and career which I will always hold dear to me.

I must also thank Dr. Hamid Ait Abderrahmane, Dr. Mustapha Amaouche, Dr. Charles Basenga Kiyanda, and Dr. Hoi Dick Ng for giving me the opportunity to work with them, to learn new things, and to apply new concepts. Thank you all for your patience and your guidance.

Last but not least, I would like to acknowledge the members on my thesis committee for reviewing my thesis and attending my examination: Dr. Nizar Bouguila, Dr. Onur Kuzgunkaya, and Dr. Hoi Dick Ng.

Giuseppe Di Labbio

June 11th, 2015

Contents

List of Figures

Nomenclature

A	Area of pipe cross-section
AR	Aspect ratio
Re_{avg}	Average Reynolds number of the systolic portion of the pulsatile velocity profile
u	Axial velocity component (velocity component in the x-direction)
μ_z	Axial velocity skewness in the z-direction
f	Body force per unit volume
x	Cartesian x-coordinate (direction shown in figure 3)
y	Cartesian y-coordinate (directed into the page from the origin in figure 3)
z	Cartesian z-coordinate (direction shown in figure 3)
B_0	Characteristic magnetic field
τ	Characteristic time scale
U_0	Characteristic velocity (chosen as inlet velocity)
C_f	Coefficient of friction
β_∞	Constant in the k-ω SST turbulence model
KE_x	Cross-sectionally averaged axial kinetic energy
KE_{yz}	Cross-sectionally averaged in-plane kinetic energy
Δke_{avg}	Cross-sectionally averaged kinetic energy difference between forced and unforced cases (per unit mass)
U	Cross-sectionally averaged velocity in the x-direction
V	Cross-sectionally averaged velocity in the y-direction
W	Cross-sectionally averaged velocity in the z-direction
$\boldsymbol{j}$	Current density vector
δ	Curvature ratio

De	Dean number
Ψ	Degree of influence
ρ	Density
∇^*	Dimensionless gradient operator
∇^{*2}	Dimensionless Laplacian operator
P^*	Dimensionless pressure
t^*	Dimensionless time coordinate
Δt^*	Dimensionless time difference
$\boldsymbol{V}^*$	Dimensionless velocity vector
y^+	Dimensionless wall distance
x^*	Dimensionless x-coordinate
y^*	Dimensionless y-coordinate
z^*	Dimensionless z-coordinate
Δt	Duration of the impact
μ	Dynamic viscosity
q	Electric charge
$\boldsymbol{E}$	Electric field vector
σ	Electrical conductivity
L_e	Entrance length
$\boldsymbol{F}$	Force vector
u_τ	Friction velocity
∇	Gradient operator
g	Gravitational acceleration

Ha	Hartmann number
D_H	Hydraulic diameter
∇^2	Laplacian operator
$\boldsymbol{B}$	Magnetic field vector
Re_{max}	Maximum Reynolds number in the pulsatile velocity profile
KE_{avg}	Normalized cross-sectionally averaged kinetic energy
D	Pipe diameter
α	Power law decay exponent
P	Pressure
R	Radius of curvature
Re	Reynolds number
ω	Specific turbulent kinetic energy dissipation rate
N	Stuart number or interaction parameter
t	Time coordinate
t_e	Time elapsed since start of impact
I	Turbulence intensity
k	Turbulent kinetic energy
ε	Turbulent kinetic energy dissipation rate
$\hat{\boldsymbol{f}}$	Unit vector in the direction of the applied body force
$\boldsymbol{V}$	Velocity vector
y_w	Wall distance
y_0	Wall distance to first gridpoint
τ_w	Wall shear stress

Abbreviations

BTAI	Blunt Traumatic Aortic Injury
CFD	Computational Fluid Dynamics
CFL	Courant-Friedrichs-Levy
DNS	Direct Numerical Simulation
KE	Kinetic Energy
MHD	Magnetohydrodynamics
PISO	Pressure Implicit with Splitting of Operator
SST	Shear Stress Transport
UDF	User-Defined Function

Chapter 1: Introduction

1.1 Overview

Motivation

Blunt traumatic aortic injury (BTAI) refers to injury of the aorta in the form of a tear or rupture brought on by blunt trauma, typically to the chest (Chapman et al. 2001); see figure 1 from Chiesa et al. (2003). It is in fact the second leading cause of death in car accidents in North America, responsible for 7,000 to 8,000 casualties per year (Pezzella & Polimenakos 2008) with 70 to 90% of patients dying on site (Chiesa et al. 2003). Despite its somewhat common occurrence, the mechanism of aortic injury in BTAI is merely postulated and it is still highly debated whether an abrupt deceleration alone is sufficient to cause aortic rupture or whether physical chest trauma is required (Chapman et al. 2001). It is this question of how fluid flows react to externally imposed accelerations which inspired this fundamental study in fluid mechanics.

Figure 1 - Illustration of blunt traumatic aortic injury (in this case aortic dissection) occurring in a car accident (Chiesa et al. 2003).

Purpose of this Study

It is interesting to note that although circular pipe flow has long been studied, especially in

the area of transition to turbulence (Eckhardt et al. 2007), very little attention has been given to how externally imposed accelerations, or body forces, affect the flow. In the sense implied by this thesis, these body forces arise in two characteristic ways, namely by geometry and by external excitation. The former includes implicit body forces arising from pipe curvature or other geometrical factors. The latter includes explicit body forces imparted onto the flow and may result from fields, such as gravitational and electromagnetic forces, from inertia arising from vessel acceleration (as in BTAI or in a centrifuge), or from other external means. In particular, it will be interesting to investigate flow behavior when subject to an impulsive body force since this will not only allow for the study of the effects of the force itself but also how the flow returns to its steady, equilibrium configuration. The purpose of this thesis therefore, is to investigate, through numerical simulation, the behavior of circular pipe flows when subjected to a localized transverse impulsive body force and to study how the flow reattains equilibrium conditions when the force ceases.

Organization of this Thesis

Since curved pipe flows and magnetohydrodynamic flows have been extensively studied over the past century, this thesis will begin by conducting a brief literature review of these topics, in sections 1.2 and 1.3 respectively, to develop some insight as to what might be expected in this study and to draw useful quantities for analysis. The question of a suitable manner of solving the governing equations then arises, and in section 1.4, a short discussion of available numerical techniques is offered, which will prove useful when discussing the methods used for solution in chapter 2. The problem is then precisely defined in section 2.1 followed by a discussion of the numerical methods in section 2.2 and of the accuracy of the results in section 2.3. Chapters 3 and 4 present the results of the study in two categories of flows, namely flows with a constant and

pulsatile inlet velocity profile respectively. Finally, in chapter 5, a summary of the main results of the study is provided and the limitations and possible future directions are discussed.

1.2 Curved Pipe Flow

Constant Curvature

Flow through curved circular pipes is perhaps the most classic problem dealing with a geometrically-induced body force on pipe flow. The first observations of the effects of curvature on fluid flow were in Thomson (1876). His observations were for the flow of a river through a bend, where he explained how the outer bank of a river washes away and the inner bank collects sediment. He also stated that the centrifugal force induces a pressure gradient in the radial direction, with the pressure increasing from the inner bend to the outer bend. At the end of his paper, he poses the question as to how pipe curvature results in losses. Eustice (1910) performed experiments on the losses exhibited in flows through curved pipes and Eustice (1911) subsequently observed the apparition of secondary fluid motion by injecting colored dye into the flow. The first theoretical analysis of steady flow through curved pipes however was conducted by Dean (1927) and further improved by Dean (1928). He obtained a series solution of the governing equations for the cross-sectional streamfunction and axial velocity in powers of the Dean number ($De = \delta^{1/2}Re$), which essentially plays the role of the Reynolds number (Re) for curved pipes as it takes into account the curvature ratio ($\delta = D/2R$; where D is the pipe diameter and R the radius of curvature). From his solution, he showed that a secondary flow develops in a plane perpendicular to the mean flow; these secondary flow structures are now commonly known as Dean vortices. Figure 2, from McConalogue & Srivastava (1968), shows isolines of the axial velocity (solid lines) and of the cross-sectional streamfunction (dashed lines) which describes the secondary flow for low (left) and moderate (right) Dean numbers. The figure shows that the

maximum axial velocity is skewed toward the outer wall of the bend (the top of the cross-section in the figure). The larger the Dean number, the more the axial velocity is skewed toward the outer wall and the further apart the Dean vortices become. As is well described by Siggers & Waters (2005), past a series of critical Dean numbers, multiple vortex solutions exist for the secondary flow arising initially from a bifurcation from the steady two-vortex solution. A more detailed review of the development of the theory of curved pipe flow can be found in Berger et al. (1983) and more recently in Verkaik (2008).

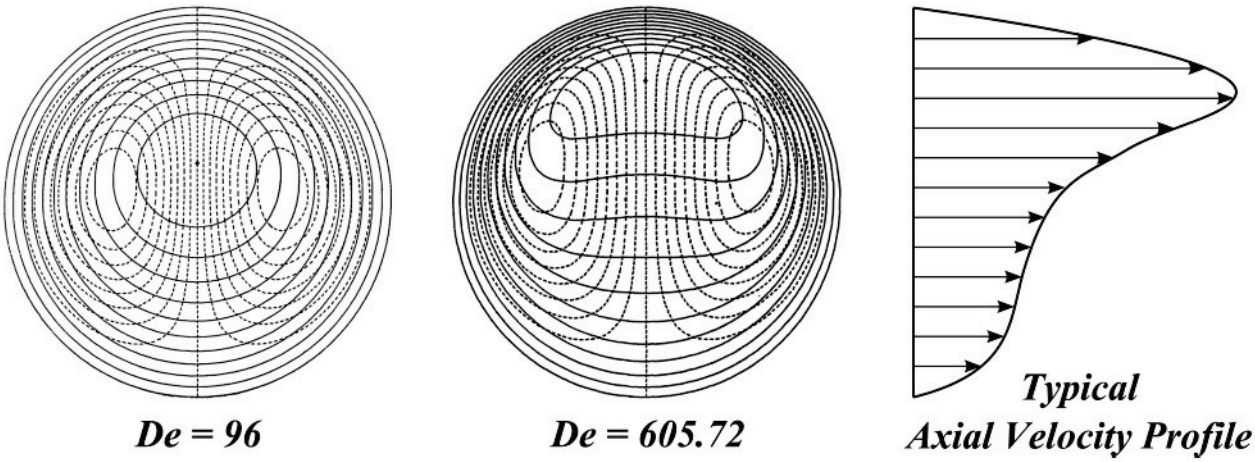

Figure 2 - Axial velocity (solid lines) and in-plane streamfunction (dashed lines) for low (left) and moderate (right) Dean numbers (McConalogue & Srivastava 1968). The outer bend of the curved pipe is located at the top of the cross-sections. A typical axial velocity profile is shown on the right, corresponding approximately to that of the *De* = 605.72 image.

Time-Varying Curvature

Although much attention has been given to the study of curved pipe flows, very few studies consider flows with time-varying curvature. An interesting example, with application to blood flow in coronary arteries, is the experimental work of Schilt et al. (1996) where a sudden variation in the radius of curvature of a U-shaped circular pipe was investigated. Aside from observing that the axial velocity profile skews toward the outer bend, it was observed that the maximum skewing occurred during the transition between minimum and maximum radii of

curvature rather than at the end states. In fact, they found that it was the dynamics of the curvature change that determined the change in skewing rather than the instantaneous radius of curvature itself. The description of the skewness of the axial velocity profile provided by Schilt et al. (1996) however is somewhat qualitative, relying on percent differences between two states. Griffith et al. (2013), although for a different cardiovascular flow application, offer a better manner of characterizing how an axial velocity profile is distorted in the direction of imposed skewing. They define the skewness in the direction z (μ_z) at a cross-section of pipe with diameter D (and area A) as a dimensionless quantity using the normalized first moment of the axial velocity u (with U denoting the cross-sectionally averaged axial velocity):

$$\mu_z = \frac{\int \frac{z}{D}\frac{u}{U}\mathrm{d}A}{\int \frac{u}{U}\mathrm{d}A} \quad where \quad U = \frac{1}{A}\int u\mathrm{d}A \tag{1}$$

With the definition above, an axial velocity profile symmetric about the plane $z = 0$ will have a skewness identically equal to zero. Furthermore, an axial velocity profile which is perfectly antisymmetric about the $z = 0$ plane (i.e. $u(-z) = -u(z)$) will have a skewness of $\pm\infty$.

1.3 Magnetohydrodynamics

Magnetohydrodynamics (MHD) is the study of electromagnetic effects in conducting fluids (Tillack & Morley 1998). It is well known from elementary physics that a point charge (q) moving through an electromagnetic field will experience the force $\boldsymbol{F} = q(\boldsymbol{E} + \boldsymbol{V}\times\boldsymbol{B})$, where $\boldsymbol{E}$ and $\boldsymbol{B}$ denote the electric and magnetic fields respectively and $\boldsymbol{V}$ the velocity field. By extension, this force, known as the Lorentz force, would be experienced by each particle of a conducting fluid in the presence of an electromagnetic field. In MHD, therefore, the equations of electromagnetism are coupled with the Navier-Stokes equations by means of a body force (Tillack & Morley 1998):

$$\rho\left(\frac{\partial \boldsymbol{V}}{\partial t}+(\boldsymbol{V}\cdot\nabla)\boldsymbol{V}\right)=-\nabla P+\boldsymbol{j}\times\boldsymbol{B}+\mu\nabla^2\boldsymbol{V}\quad where\quad \boldsymbol{j}=\sigma(\boldsymbol{E}+\boldsymbol{V}\times\boldsymbol{B}) \tag{2}$$

Where ρ denotes the fluid density, P the pressure, $\boldsymbol{j}$ the current density, μ the dynamic viscosity of the fluid, and σ the electrical conductivity. Of course there are other equations governing MHD flows, namely arising from Maxwell's equations, however it is not necessary to describe them here.

Characterization of MHD Flows

As the Dean number is used to characterize curved pipe flows, it is common in MHD to characterize a flow using its Hartmann number (*Ha*), which is a ratio of magnetic to viscous forces, and its interaction parameter or Stuart number (*N*), a ratio of magnetic to inertial forces (Tillack & Morley 1998).

$$Ha = B_0 D\sqrt{\frac{\sigma}{\mu}} \tag{3}$$

$$N = \frac{\sigma B_0^2 D}{\rho U_0} \tag{4}$$

With B_0 and U_0 representing some characteristic magnetic field and velocity in the flow respectively.

Generalizing the Interaction Parameter

The interaction parameter is particularly interesting to this study as it describes the interaction between a body force per unit volume (*f*) and the flow's inertia. The interaction parameter can be generalized to arbitrary body forces acting on any flow through the use of common analogies between electromagnetism and fluid mechanics, such as charge representing volume and current representing volume flow rate (Ottesen et al. 2004). It can be shown that the magnetic field is analogous to a body force per unit volume per unit velocity (f/U_0; i.e. from $\boldsymbol{F} = q(\boldsymbol{E} + \boldsymbol{V}\times\boldsymbol{B})$) and the electrical conductivity is analogous to the inverse (U_0/f). The electrical

conductivity can be thought of as the amount of current a material can draw per unit area in an electric field of unit strength ($E \sim f$; i.e. from $\boldsymbol{F} = q(\boldsymbol{E} + \boldsymbol{V}\times\boldsymbol{B})$), or by analogy, the volume flow rate that can be drawn per unit area (i.e. the average velocity) in the presence of a force per unit volume of unit strength. With these analogies, the quantity Ψ, which will be referred to as the degree of influence, is derived by direct substitution of the analogous terms in equation 4 and describes the relative strength of the body force compared with the flow inertia. The same result could easily be obtained from Buckingham's π theorem with the appropriate choice of variables.

$$\Psi = \frac{fD}{\rho U_0^2} \tag{5}$$

The previous two sections focused on discussing literature similar to the problem under study to gain some physical insight as to what may be expected. Since the governing equations of fluid motion, namely the continuity and Navier-Stokes equations, have not been solved for the general case, the question then arises as to how to treat the problem of this study. Some key numerical methods presently available in computational fluid dynamics (CFD) are therefore offered in the following section.

1.4 Numerical Techniques

Nature of a Turbulent Flow

It is well-known that the laminar velocity profile for circular pipe flow is linearly stable for all Reynolds numbers (Salwen et al. 1980, Eckhardt et al. 2007). This implies that laminar flow in a circular pipe will only experience transition to turbulence if a perturbation to the flow is strong enough for a given Reynolds number. Kerswell (2005) notes that the lowest critical Reynolds number for which transition could occur in pipe flow is quoted in the literature to range from 1,760 to 2,300. Furthermore, a continuous perturbing mechanism (such as wall roughness for a large enough flow rate) is required in order to sustain a turbulent flow (Wilcox 1994),

otherwise any excess energy will be dissipated by the energy cascade and the flow will return to its stable laminar state.

Direct Numerical Simulation

The inlet Reynolds numbers considered in this study range from 0 to 6,358 and due to the magnitude and nature of the body force, transition to turbulence is likely to occur. The problem therefore encompasses the laminar, transitional, and turbulent regimes. Ultimately, the best way to treat such a problem would be through direct numerical simulation (DNS). In DNS, no *a priori* assumptions are made regarding the nature of the flow and the Navier-Stokes equations are solved exactly (Versteeg & Malalasekera 2007). Unfortunately, DNS requires a grid and time resolution fine enough to capture the characteristic length and time scales of the smallest eddies in a turbulent flow (the Kolmogorov scales). This limits the use of DNS to low Reynolds number flows with a sufficiently small domain size. Due to its limitations, including the computational resources and time required to perform such simulations, a turbulence modeling approach is often used. The most noteworthy turbulence models that have the capability of dealing with flows encompassing the three flow regimes are the k-ω SST model and the transition SST model (with SST meaning shear stress transport).

Turbulence Models for Low Reynolds Number Flows

What is known today as the standard k-ω model was developed by Wilcox (1988); here k denotes the turbulent kinetic energy, $\omega = \varepsilon/k$ the specific turbulent kinetic energy dissipation rate, and ε the turbulent kinetic energy dissipation rate. This model has the benefit of accurately describing the boundary layer down to the viscous sublayer, which was quite appealing since the standard k-ε model, devised by Launder & Sharma (1974), cannot accurately handle wall bounded flows without the use of wall functions or modifications introduced in later years.

Despite the standard k-ω model's accuracy in the boundary layer, the model is sensitive to freestream values of ω, usually resulting in over-prediction of turbulence levels in the freestream. It was Menter (1993) who appealed to this deficiency (and others) with the development of the k-ω SST model (later improved by Menter et al. 2003a and Menter et al. 2003b). The model blends the standard k-ω model in the boundary layer with the standard k-ε model in the freestream, essentially using the strengths of the two models to develop one that is more accurate, stable, and robust. Further, Menter et al. (2006) developed the transition SST model, which couples the k-ω SST model with two additional correlation-based transport equations; one for the transition onset Reynolds number and one for the intermittency (which is essentially a trigger for the transition process and is analogous to an induction variable for chemical reactions). Although the model is known to do better in predicting transition, it requires a fine mesh resolution close to the wall (Menter et al. 2006) and the additional two equations combined with the continuity and Navier-Stokes equations result in a total of eight differential equations to be solved and would therefore require significantly more computational resources than the k-ω SST model alone.

Adequacy of the k-ω SST Model

Nonetheless, the k-ω SST model has often been shown to give adequate results. The model has a considerably reduced sensitivity to y^+ values of the first gridpoints away from the wall, owing to Menter et al. (2003b) who developed a set of "automatic" wall functions in the sense that they are incorporated in the model constants; y^+ is the dimensionless wall distance and is given by $\rho u_\tau y_w/\mu$ (where ρ is the fluid density, y_w the distance from the wall, μ the fluid's dynamic viscosity, and u_τ the friction velocity given by $\sqrt{\tau_w/\rho}$ with τ_w being the wall shear stress. They also demonstrated excellent agreement with experimental data for three test cases with first gridpoints ranging from $y^+ = 0.1$ to as far out as $y^+ = 100$. In particular, studies of cardiovascular

flows, exhibiting a similar range of Reynolds numbers as considered in this study, such as Ghalichi et al. (1998), Ryval et al. (2004), Keshavarz-Motamed & Kadem (2011), and Keshavarz-Motamed et al. (2013) used the k-ω SST model and reported good agreement of their results with experimental data for a variety of flow conditions.

Chapter 2: Methodology

2.1 Problem Definition

Geometrical and Fluid Parameters

As this study was motivated by BTAI, some parameters used for numerical simulation will be modeled according to those commonly seen in such cases. This study consists of a straight, rigid, impermeable pipe of circular cross-section with diameter D = 0.022 m, which is typical of a human aorta (Boiron et al. 2007, Keshavarz-Motamed & Kadem 2011). The working fluid was modeled as incompressible and Newtonian with the density (ρ) and dynamic viscosity (μ) corresponding to those of blood, namely 1050 kg/m^3 and 0.0035 Pa·s respectively (Morris et al. 2005).

Application of the Body Force

Two different categories of flows are considered, namely flows with a constant inlet velocity and flows with a pulsatile inlet velocity. In either case, the inlet velocity profile is spatially uniform and the body force is applied for a short duration on a localized volume of fluid where the flow has fully developed. The body force magnitude and duration were selected to be within the range typically experienced in BTAI, namely 15-150ρg of force per unit volume acting for 50-100 ms (Chapman et al. 2001, Lee 2008). The body force per unit volume (f) was therefore selected as a rectangular impulse in time and space with a magnitude of 500,000 N/m^3. For the uniform flow case, three inlet Reynolds numbers are simulated, namely 1500, 3000, and 5500 with an impact occurring at t = 0.100 s for a duration (Δt) of 95 ms. For the pulsatile flow case, a physiological pulsatile velocity profile simulating the contraction period of the heart (systole) is used (Re_{max} = 6358 and Re_{avg} = 4291 over 0 s < t < 0.300 s). Impacts are tested during the accelerating, peak, and decelerating phases of the profile with impact durations of 95 ms (0.040 s

to 0.135 s), 90 ms (0.135 s to 0.225 s), and 95 ms (0.190 s to 0.285 s) respectively.

Boundary and Initial Conditions

The uniform flow cases were initialized from the steady unforced solution (i.e. Hagen-Poiseuille flow) and the pulsatile cases were initialized from rest. In all cases, the no-slip and no-penetration conditions are in effect at the pipe walls. A Neumann boundary condition is also used at the outlet, implying that gradients of fluid variables in the direction normal to the outlet plane vanish. See figure 3 below for a schematic of the problem under study.

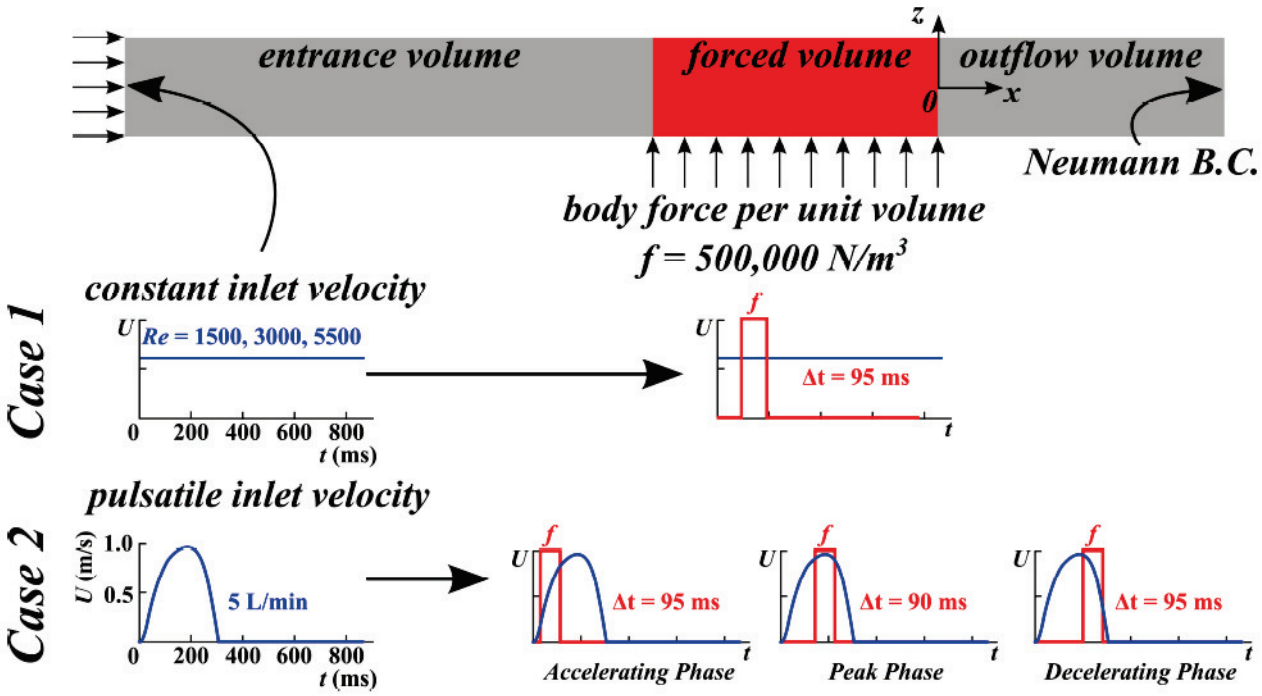

Figure 3 - Schematic of the problem under study. Three Reynolds numbers are tested for a constant inlet velocity profile and three different impact locations are tested for a pulsatile inlet velocity profile.

Coordinate System and Domain Length

For convenience, a dimensionless coordinate system is developed here to avoid discussing the different starting positions and impact durations used throughout the study. The dimensionless time coordinate is defined as $t^* = t_e/\Delta t$, with t_e being the time elapsed since the moment of impact. With this definition, the moment of impact is given by $t^* = 0$ and the end of

impact by $t^* = 1$. Similarly, the dimensionless spatial coordinates can be obtained through normalization with the diameter, i.e. $x^* = x/D$, $y^* = y/D$, and $z^* = z/D$. The forced and outflow volumes were each selected to have a length of 0.3 m. The outflow length was selected by starting with a long outflow length to ensure the Neumann boundary condition applied (1.5 m). The length was gradually reduced until a difference of up to 0.5% was observed in the velocity field with the original long length. The significant reduction in outflow length owes to the nature of the boundary condition which only requires that gradients normal to the outlet plane vanish and not gradients within the outlet plane. With the location of the origin shown in figure 3, the forced volume is bounded by $-13.63 < x^* < 0$ and the outflow volume by $0 < x^* < 13.63$. A long enough entrance length is provided for fully developed flow to exist where the body force is applied. According to classical fluid mechanics texts, laminar and turbulent pipe flows require entrance lengths of $L_e = 0.06DRe$ and $L_e = 4.4DRe^{1/6}$ respectively to fully develop (Munson et al. 2013); since these are empirical relations, an additional 50% of the computed entrance lengths were added in what follows. For the constant inlet velocity profile with $Re = 1500$, a laminar model is used since turbulence has not been observed for $Re < 1760$ in pipe flow and the entrance length was selected as 3.0 m ($136.4D$). For all other cases, a turbulence model is used, and since the maximum inlet Re simulated is 6358 for the peak of the pulsatile inlet velocity profile, the entrance length was selected as 0.6 m ($27.3D$). With t^* and x^* defined, the body force per unit volume acting in the positive z direction (figure 3) may be expressed mathematically:

$$f = \begin{cases} 500{,}000 N/m^3 & -13.63 < x^* < 0 \quad and \quad 0 < t^* < 1 \\ 0 N/m^3 & otherwise \end{cases} \tag{6}$$

The governing equations in this study are the continuity and Navier-Stokes equations. Using the dimensionless parameters previously defined, these conservation equations can be nondimensionalized as:

$$\nabla^* \cdot \boldsymbol{V}^* = 0 \quad and \quad \tau \frac{\partial \boldsymbol{V}^*}{\partial t^*} + \left(\boldsymbol{V}^* \cdot \nabla^*\right)\boldsymbol{V}^* = -\nabla^* P^* + \Psi \hat{\boldsymbol{f}} + \frac{1}{Re}\nabla^{*2}\boldsymbol{V}^* \tag{7}$$

$$\boldsymbol{V}^* = \frac{\boldsymbol{V}}{U_0} \quad \nabla^* = D\nabla \quad \tau = \frac{D/U_0}{\Delta t} \quad P^* = \frac{P}{\rho U_0^2} \quad \Psi = \frac{fD}{\rho U_0^2} \quad Re = \frac{\rho U_0 D}{\mu} \tag{8}$$

2.2 Numerical Method

The governing equations were solved numerically using the commercial computational fluid dynamics software ANSYS FLUENT 12.1.4, which uses a finite volume approach. A laminar model was used for the uniform inlet velocity profile with Re = 1500 and the k-ω SST model was used for all other cases owing to the discussion in section 1.4. The time step was selected as 0.01 s before the impact and reduced to 0.005 s during and after the impact. The choice of the time step is described further in section 2.3. A segregated (or decoupled) pressure-based solver was used as opposed to a density-based solver since this study is for an incompressible flow and variations in density are negligible. Pressure and velocity are coupled using the PISO scheme. This scheme has the added benefit of satisfying the continuity and momentum equations more closely (making use of what is known as the neighbor or momentum correction) and is widely suggested in the literature for transient problems as it has high accuracy and reduces the number of iterations required for convergence at each time step (Versteeg & Malalasekera 2007). The PISO scheme also incorporates a pressure correction near skewed cells (though, as shown in section 2.3, this is not necessary for the mesh used). Gradients of fluid variables at the faces of cells were computed using a least-squares cell-based approximation, which assumes that the variation of the solution between cell centers is linear. The momentum, turbulent kinetic energy, and specific dissipation rate equations were spatially discretized using second-order upwind schemes. Time was discretized using a first-order implicit scheme which is stable for any choice of time step (hence no CFL condition must be satisfied) and does not exhibit numerical diffusion

as for explicit first-order schemes (LeVeque 2002, Celik 2008). The body force was applied using a user-defined function (UDF); refer to the appendix. As the body force is rather large in this study, a body-force-weighted pressure interpolation scheme was used to compute pressure at the faces of cells. The scheme treats the body force as part of the pressure gradient term in the Navier-Stokes equations and works best when the body force is know *a priori* (ANSYS Inc. 2009). This approach has been used with successful experimental validation in convective heat transfer problems involving substantial body forces (such as buoyancy for large temperature gradients) by Chandratilleke & Nadim (2012) and Rout et al. (2012). The convergence criterion was based on whether the absolute residuals for the continuity, momentum, turbulent kinetic energy, and specific dissipation rate equations all fell below 10^{-5}. A lower residual tolerance (10^{-8}) was tested with no significant difference in the results observed (up to 0.002% difference in the velocity field).

Additional Boundary Conditions

The cases using the k-ω SST model require specification of two additional boundary conditions since two additional transport equations are introduced. FLUENT allows specification of the turbulence intensity (I) and hydraulic diameter (D_H) as the boundary conditions at the inlet (suggested for internal flows by ANSYS Inc. 2009). From these values, the turbulent kinetic energy can be estimated from:

$$k = \frac{3}{2}(U_0 I)^2 \tag{9}$$

$$\omega = \frac{k^{1/2}}{\beta_\infty^{1/4} D_H} \quad where \quad \beta_\infty = 0.09 \tag{10}$$

For this study, the hydraulic diameter is simply equal to the diameter of the pipe (0.022 m) and a low turbulence intensity of 1% was selected since one would not expect the flow to exhibit much turbulent fluctuations at the inlet prior to the impact.

2.3 Meshing Procedure and Independence Study

Near-Wall Meshing

With the physical and computational models devised, a suitable mesh is needed to attain adequate accuracy for a reasonable computation time. A completely polar mesh is not suitable as a face mesh due to the high skewness of the cells at the center of the cross-section. Instead, a polar mesh is only used close to the boundary layer and a near-uniform mesh is used toward the center of the cross-section. A smoothed coupling between the two meshes is achieved using GAMBIT's tri-primitive meshing algorithm. As explained in section 1.4, the k-ω SST model has significantly less restriction on the y^+ of the first gridpoints, however it is best to have the first gridpoint within the viscous sublayer ($y^+ < 5$) especially in cases with adverse pressure gradients since the flow in this layer is most readily affected (Menter et al. 2003b, Versteeg & Malalasekera 2007, Menter 2009). An estimation for the first layer thickness can be obtained from the definition of y^+ (i.e. $y_0 = \mu y^+/\rho u_\tau$), making use of the Blasius formula for the coefficient of friction for a turbulent internal flow ($C_f = 0.079Re^{-0.25}$), where wall shear stress is given by $\tau_w = {}^1/_2 C_f \rho U^2$ (equations from Munson et al. 2013). The equations of course do not consider the body force which will certainly increase the wall shear stress observed (and hence reduce the first layer thickness required), therefore in order to obtain $y^+ < 5$, an undershoot is used; $y^+ = 1$ for instance results in a first layer thickness of approximately $5 \cdot 10^{-5}$ m. Using a first layer thickness of $5 \cdot 10^{-5}$ m ultimately resulted in a maximum observed y^+ value for the first gridpoint of 2.8 after all simulations.

Final Mesh

The final mesh, after the grid-convergence study (described below), consisted of 163,200 hexahedral elements (see figure 4). The mesh configuration was similar to that used by Lee

(2008), which was validated against experimental data for Hagen-Poiseuille and Womersley flows in an elastic pipe. A growing boundary layer mesh was used with a growth rate of 1.3 (30%) with 32 angular divisions. It can be noted from figure 4 that the aspect ratio in the first layer is quite large (AR = 43), however the grid-convergence study demonstrates that this does not harm the accuracy of the simulations since changes in the radial direction are most important and resolved whereas changes in the azimuthal direction are small in the boundary layer. It can also be noted that the cells have small skewness which results in an efficient mesh; cell skewness is defined with regard to asymmetries in cell angles and can lead to difficulties in convergence (ANSYS Inc. 2009). With regard to the flow direction, the entrance length was divided using 6 mm per division. The forced and outflow volumes were meshed twice as fine, since these are the regions of interest, with 3 mm per division.

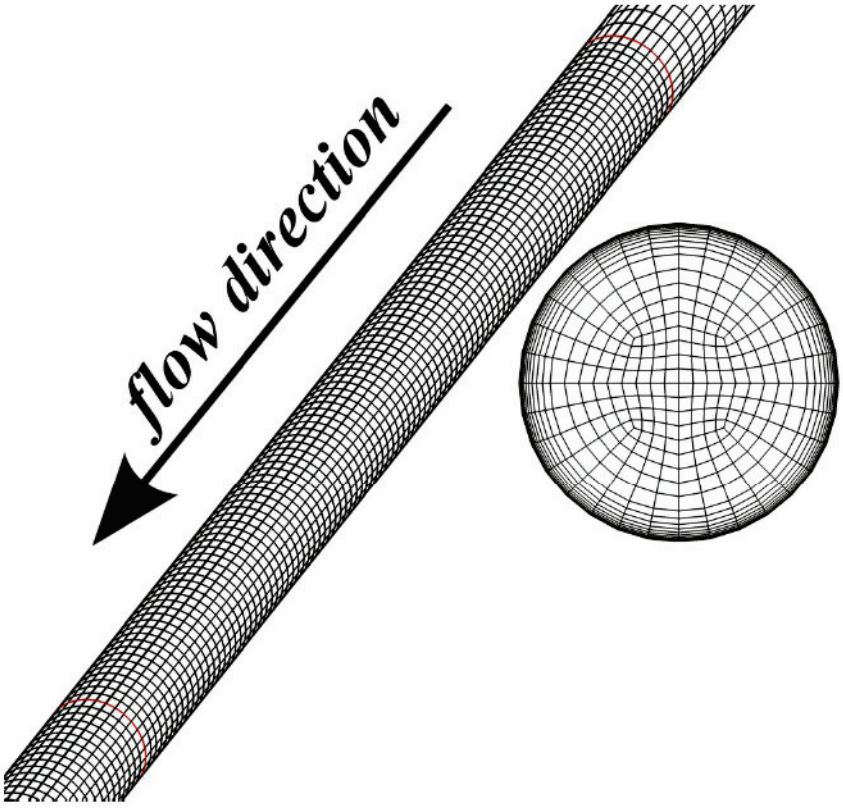

Figure 4 - Face mesh used for all simulations. Mesh consists of 163,200 hexahedral elements after the grid convergence study.

Grid and Time Convergence Studies

The grid convergence study was performed for a constant inlet velocity profile with Re = 5500. Using a constant inlet flow is expected to exhibit more difficulty in convergence than using a pulsatile inlet flow since the background velocity field does not decay and the body force should therefore have a more substantial effect. In order to ensure the results were grid-converged, three successively fine meshes were constructed with a refinement ratio of approximately 1.4 (Celik et al. 2008 suggests 1.3 or higher) and with the total number of elements amounting to 163,200, 547,200, and 1,522,800. A fine time step (0.001 s) was used for each simulation. The evolution of cross-sectionally averaged kinetic energy and axial skewness are of particular interest in this study, and are used as criteria to judge grid convergence. The error in these quantities are observed to be less than 6% between the coarsest and finest meshes on average, with errors in the velocity field being as much as 3%. Figure 5 shows the section with the largest error (x^* = 0.90) in the cross-sectionally averaged kinetic energy and axial skewness. The peak error in kinetic energy of 10.5% occurs near the end of the impact (t^* = 0.84). One must keep in mind that these quantities are cross-sectional averages and therefore pose a very strict convergence criterion. In particular, the cross-sectionally averaged kinetic energy contains the sum of the squared errors of the three velocity components which is summed over each gridpoint in the cross-section. The axial velocity profile at t^* = 0.84 is also plotted at x^* = 0.90 in figure 5 with a corresponding maximum error of 4.7%. The accuracy of the mesh with 163,200 elements was therefore judged sufficient and was ultimately selected. With the mesh selected, time steps of 0.001 s, 0.005 s, and 0.01 s were tested. Before the body force was applied, less than 0.03% error was observed in the velocity field between the coarsest and finest time steps. During and after application of the body force, less than 0.18% error was observed

between the time steps of 0.001 s and 0.005 s. In light of these results, a time step of 0.01 s was used prior to application of the body force and the time step was reduced to 0.005 s during and after the impact to acquire more data for analysis.

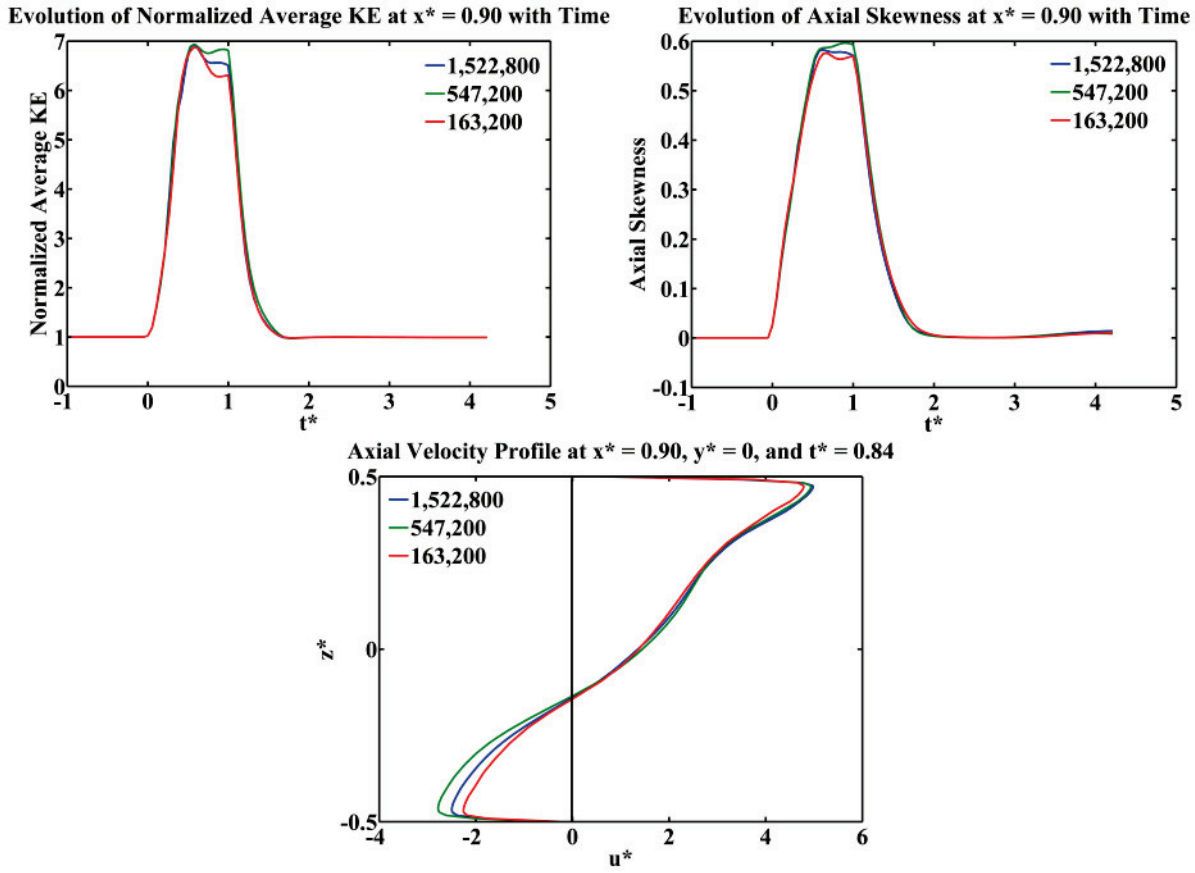

Figure 5 - Cross-sectionally averaged kinetic energy and axial skewness at $x^* = 0.90$ for a constant uniform inlet velocity profile with $Re = 5500$. The largest errors observed occur near the end of the impact at $t^* = 0.84$ and are 10.5% for the normalized average kinetic energy, 6% for the axial skewness, and 4.7% for the axial velocity.

Chapter 3 : Constant Inlet Velocity

Prior to application of the body force, the fluid has attained steady-state conditions. At the moment the impulsive body force is applied, a transverse pressure gradient develops in the forced volume, acting in the opposite direction of the force and equal in magnitude. For a pressure gradient of 500,000 N/m^3 acting across the pipe diameter of 0.022 m, a pressure difference of 11 kPa is seen between the top and bottom of the forced volume (compared to 0.23 kPa for gravity acting alone). The induced high pressure at the top of the pipe (positive z^*) generates a pressure gradient between the forced and unforced pipe sections, resulting in the fluid being pushed out of the forced volume (see figure 6). The inverse effect, flow entering the forced volume, can be noticed at the bottom of the pipe (negative z^*).

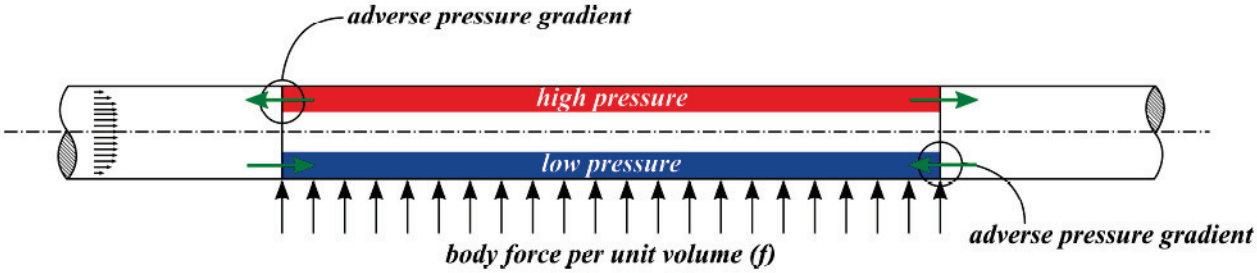

Figure 6 - Schematic of the transverse pressure gradient induced by the action of the body force causing fluid to flow out of the forced volume at the top of the pipe and inward at the bottom.

3.1 Velocity Field

From the two sites of adverse pressure gradient at the boundaries of the forced volume (x^* = -13.63 and 0), two streamwise counter-rotating vortices develop and gradually move toward the pipe centerline as they grow. In fact, the effect of the body force is seen to be localized around the boundaries of the forced volume, and the flow in the center of the forced volume remains unperturbed for much of the impact duration. Figure 7 shows the two vortices for the Re = 5500 case at approximately mid-impact (t^* = 0.53).

Pressure Contours (t* = 0):

Velocity Field (t* = 0.53):

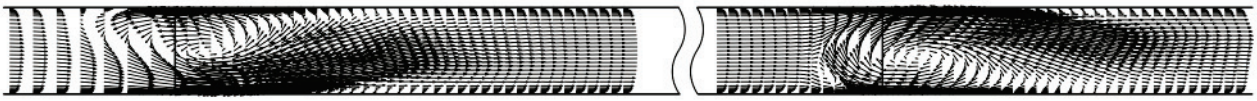

Figure 7 - Pressure contours at the moment of impact ($t^* = 0$) and velocity field near mid-impact ($t^* = 0.53$) showing the two counter-rotating streamwise vortices for the $Re = 5500$ case. Notice the "wave-like" propagation and spatial decay of the high axial velocity flow issuing from the streamwise vortices.

The streamwise vortices for all three cases (Re = 1500, 3000, and 5500) are depicted in figure 8 along with the secondary flow. It can be seen from the figure that the body force has a more substantial effect on the Re = 1500 case; stronger streamwise vortices develop at the boundaries of the forced volume compared to the higher Re cases. This can be explained by higher values of the parameter $\Psi = fD/\rho U_0^2$. The parameter Ψ can be thought of as a ratio of the transverse pressure gradient to the streamwise pressure gradient. The larger the value of Ψ, the more the transverse pressure gradient dominates the streamwise pressure gradient.

As the streamwise vortices develop, secondary flows develop in the same regions simultaneously. Figure 8 also shows the secondary flow with normalized axial velocity contours of two selected sections (x^* = -12.72 and 0.90) at three selected times (t^* = 0.53, 1.05, and 1.26) for each case. For ease of viewing, the secondary flow vectors were normalized with respect to the maximum magnitude of the secondary flow for each given cross-section at each instant.

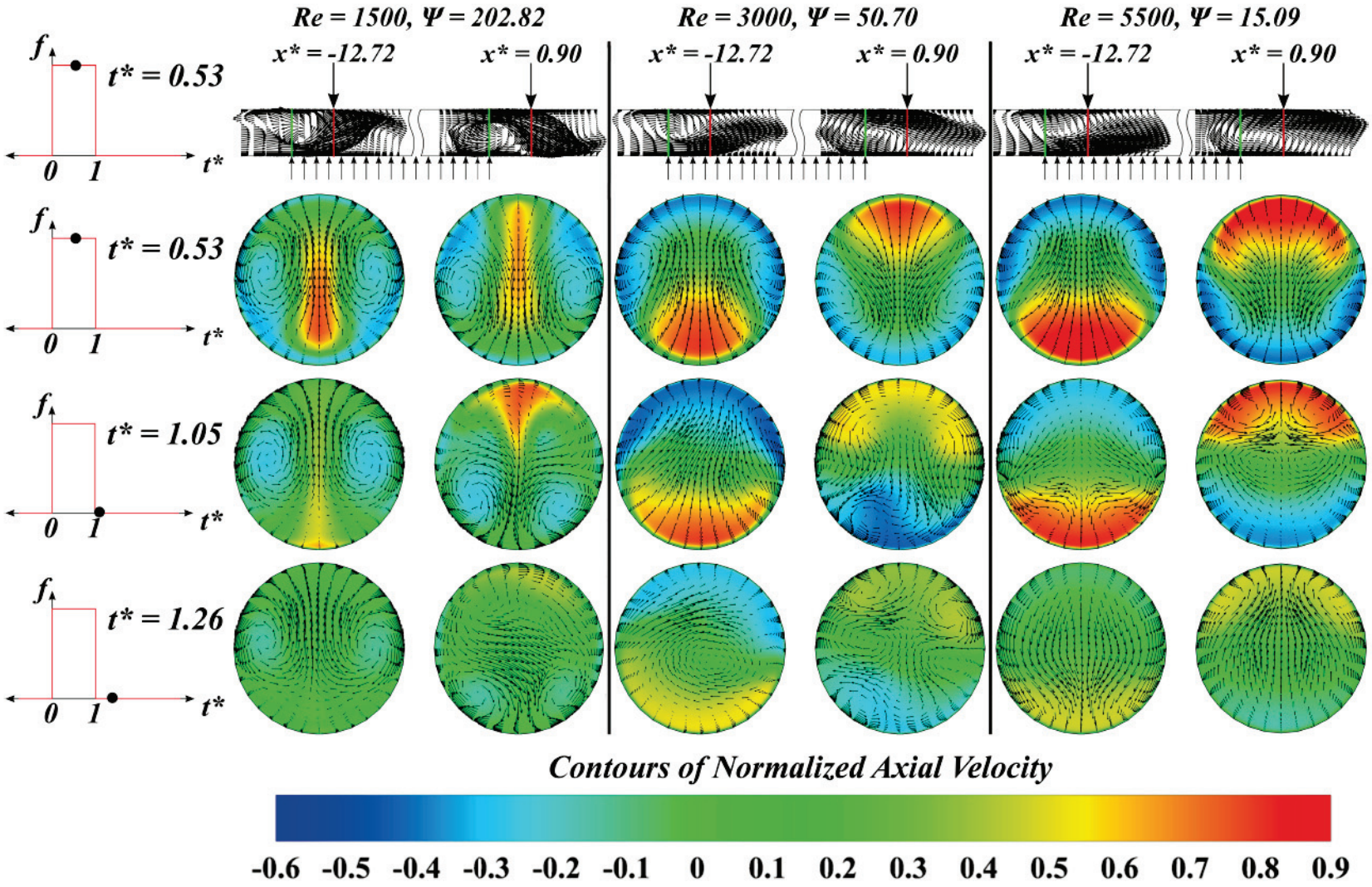

Figure 8 - Secondary flow and contours of normalized axial velocity for Re = 1500, 3000, and 5500 at t^* = 0.53, 1.05, and 1.26. Two streamwise counter-rotating vortices can be seen during the impact at t^* = 0.53 with secondary flows appearing as Dean-like vortices. After the impact (at t^* = 1.05 and 1.26 for example), more complex secondary flow structures develop to effectively reattain the steady-state flow configuration.

For the upstream section ($x^* = -12.72$), high axial velocity occurs at the bottom of the pipe, where the low pressure draws the fluid inward, whereas it occurs at the top of the pipe at the downstream section ($x^* = 0.90$), where the high pressure forces the flow outward. During the impact ($0 < t^* < 1$), the secondary flows are Dean-like vortices which carry the fluid from the high axial velocity regions to the near-wall region, effectively slowing it down in an attempt to attain equilibrium conditions. The $Re = 5500$ case is seen to attain steady conditions more rapidly than the lower Re cases as the secondary structures are quickly carried downstream and dissipate their energy. For $Re = 1500$, the Dean-like vortices tend to persist for a longer duration. Most interesting is the $Re = 3000$ case, where more intricate structures are seen (6 weak secondary vortices can be seen for $x^* = 0.90$ at $t^* = 1.26$ as opposed to 1 vortex at $x^* = -12.72$ at the same instant), however they are short-lived.

3.2 Axial Skewness

The impulsive body force perturbs the velocity profile spatially and temporally. The skewness of the three-dimensional axial velocity profile for a given cross-section can be quantified as done by Griffith et al. (2013) in their investigation of the effects of stenotic flows with eccentric stenosis (see equation 1). Figure 9 shows contours of axial skewness (μ_z) as a function of time and space as well as the evolution of axial skewness at six selected upstream sections ($x^* = -13.63$, -13.18, -12.72, -11.81, -10.90, and -10.45) and six selected downstream sections ($x^* = 0$, 0.45, 0.90, 1.81, 2.72, and 3.18) for each case. From the contours, it can be seen that the effects of the body force are localized around the boundaries of the forced volume with skewness peaks occurring near these boundaries. The lower the Reynolds number, the more localized the effects are and the larger the peaks in skewness.

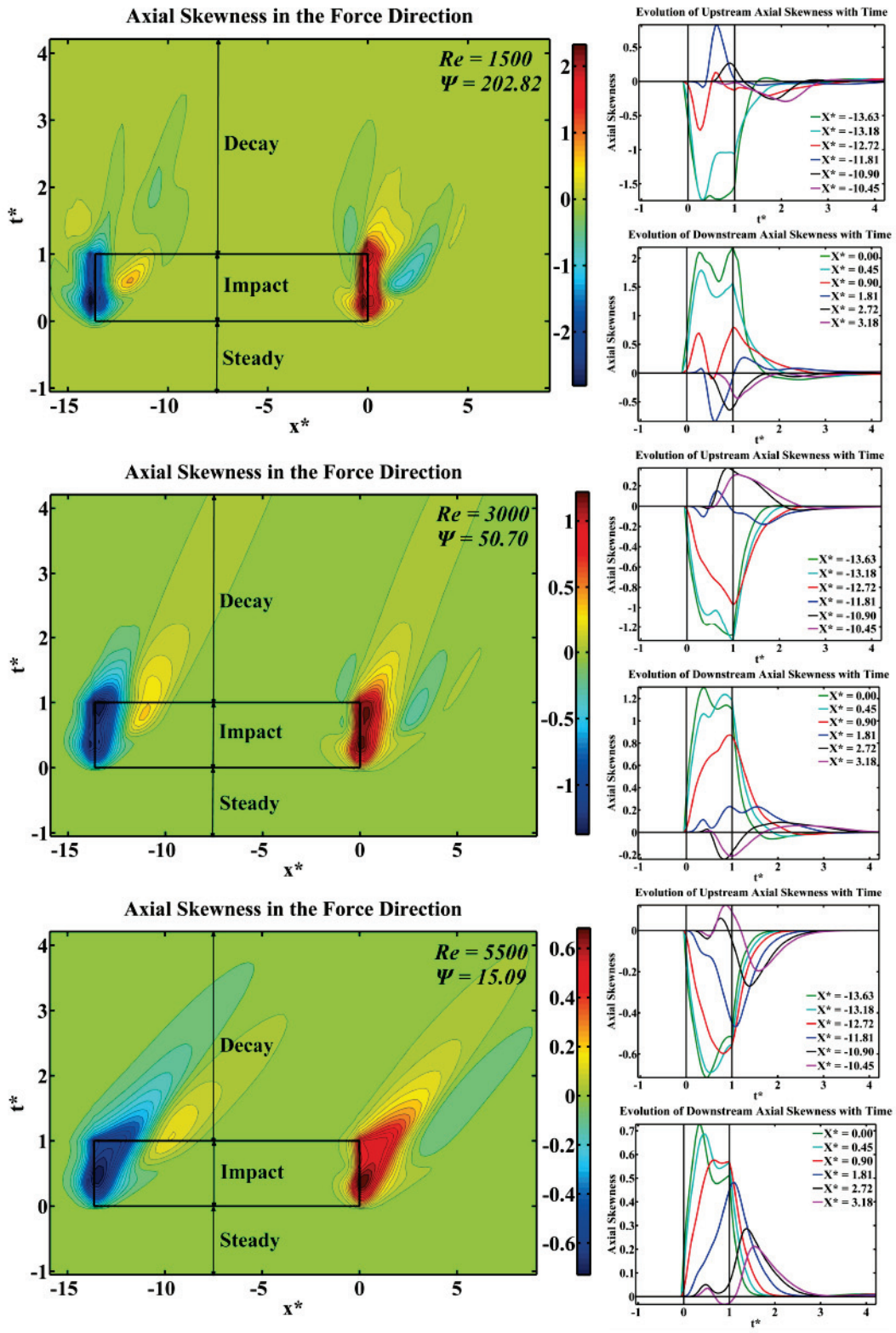

Figure 9 - Contours of axial skewness for *Re* = 1500, 3000, and 5500 and plots at different sections along the pipe. The effects of the body force are localized at the boundaries of the forced volume and the further a section from the boundaries, the lesser the skewness it experiences. The skewness decays as it propagates downstream at a speed proportional to *Re*.

The maximum skewness for sections near the boundaries of the forced volume occurs during the impact (not at the end of the impact). This is similar to the experimental observation of Schilt et al. (1996), namely that for flow in a U-shaped tube with time-varying curvature, the maximum skewness occurred during the curvature change rather than at the final states. The development of the two streamwise counter-rotating vortices and the secondary flow at these locations is the main contribution to the skewing. The propagation of these features downstream corresponds to propagation of the skewness downstream. When the body force ceases, the skewness continues to propagate downstream and decays with time, just as the streamwise vortices and secondary flows do. This is also seen in the form of a decaying wave from the velocity field in figures 7 and 8. The three contour plots have identically scaled axes and as such the speed of propagation of the skewness can clearly be seen to be larger with larger Reynolds numbers. It can also be seen that sections further away from the boundaries of the forced volume experience changes in skewness at later times and the further the section from the boundaries of the forced volume, the lesser the skewness it experiences. In fact, sections far enough downstream from the boundaries of the forced volume only experience changes in skewness after the impact. In order of increasing *Re*, 62%, 42%, and 37% of the forced volume and sections with $x^* > 5.23$, 5.68, and 7.05 experienced changes in skewness after the impact (i.e. after $t^* = 1$). The sign of the skewness is positive for sections near the downstream boundary since high axial velocity exists at the top of the pipe (positive z^*), and negative near the upstream boundary due to the high axial velocity being at the bottom of the pipe (negative z^*).

3.3 Kinetic Energy

In figure 10, contour plots of normalized cross-sectionally averaged kinetic energy (KE_{avg}) and its evolution at three selected upstream ($x^* = -13.63$, -12.72, and -10.45) and three selected

downstream ($x^* = 0$, 0.90, and 3.18) sections are shown for the three cases. The kinetic energy is normalized with respect to the cross-sectionally averaged kinetic energy of the respective steady unforced case. A value of $KE_{avg} = 1$ therefore corresponds to the kinetic energy of the base flow.

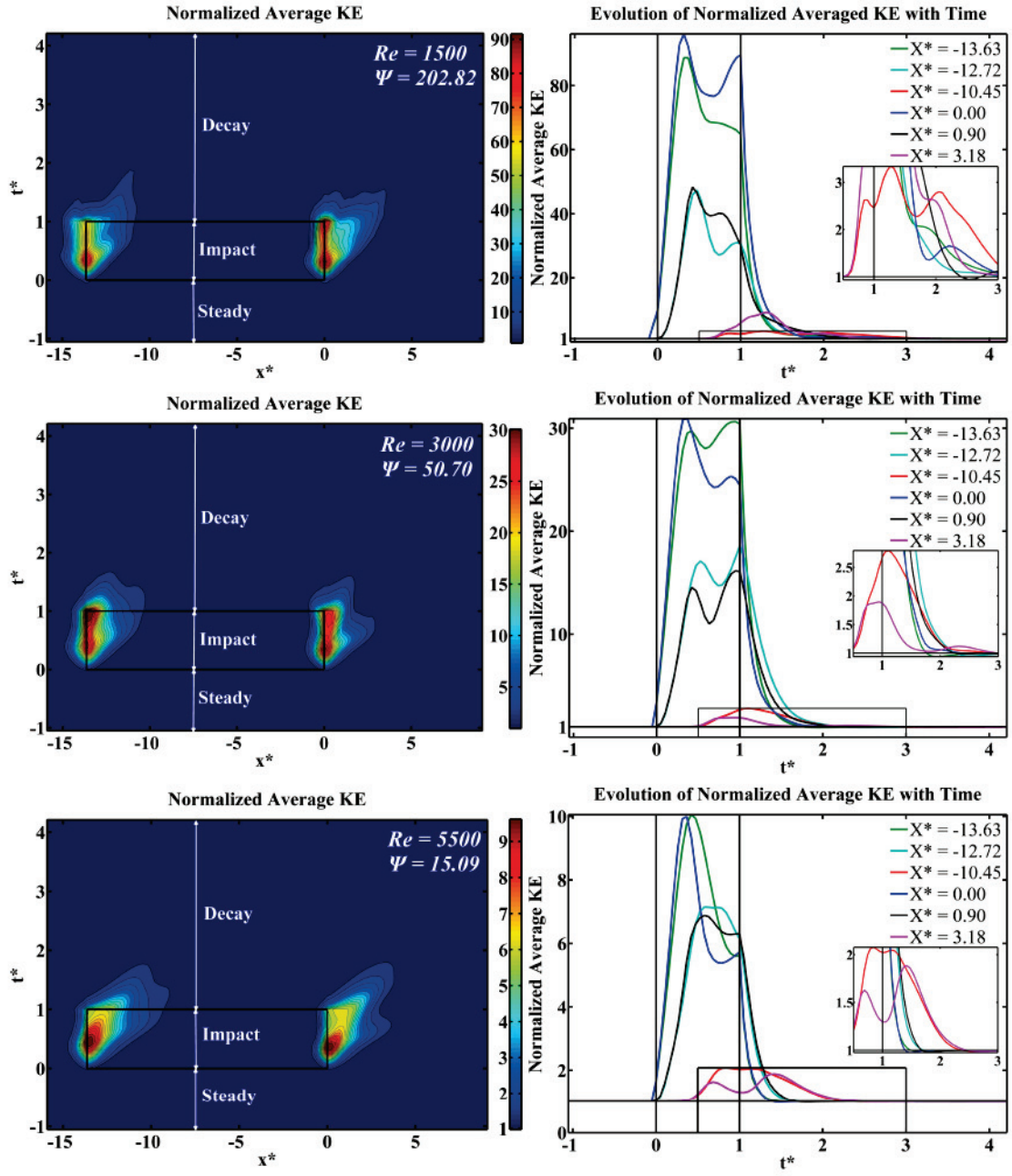

Figure 10 - Contours of normalized average kinetic energy for $Re = 1500$, 3000, and 5500 and plots at different sections along the pipe. The body force has the greatest effect for $Re = 1500$, with the cross-sectionally averaged kinetic energy rising 90 times its steady-state value in comparison to 10 times for $Re = 5500$. The temporal decay of kinetic energy is quicker for larger Re whereas the spatial decay is quicker for lower Re.

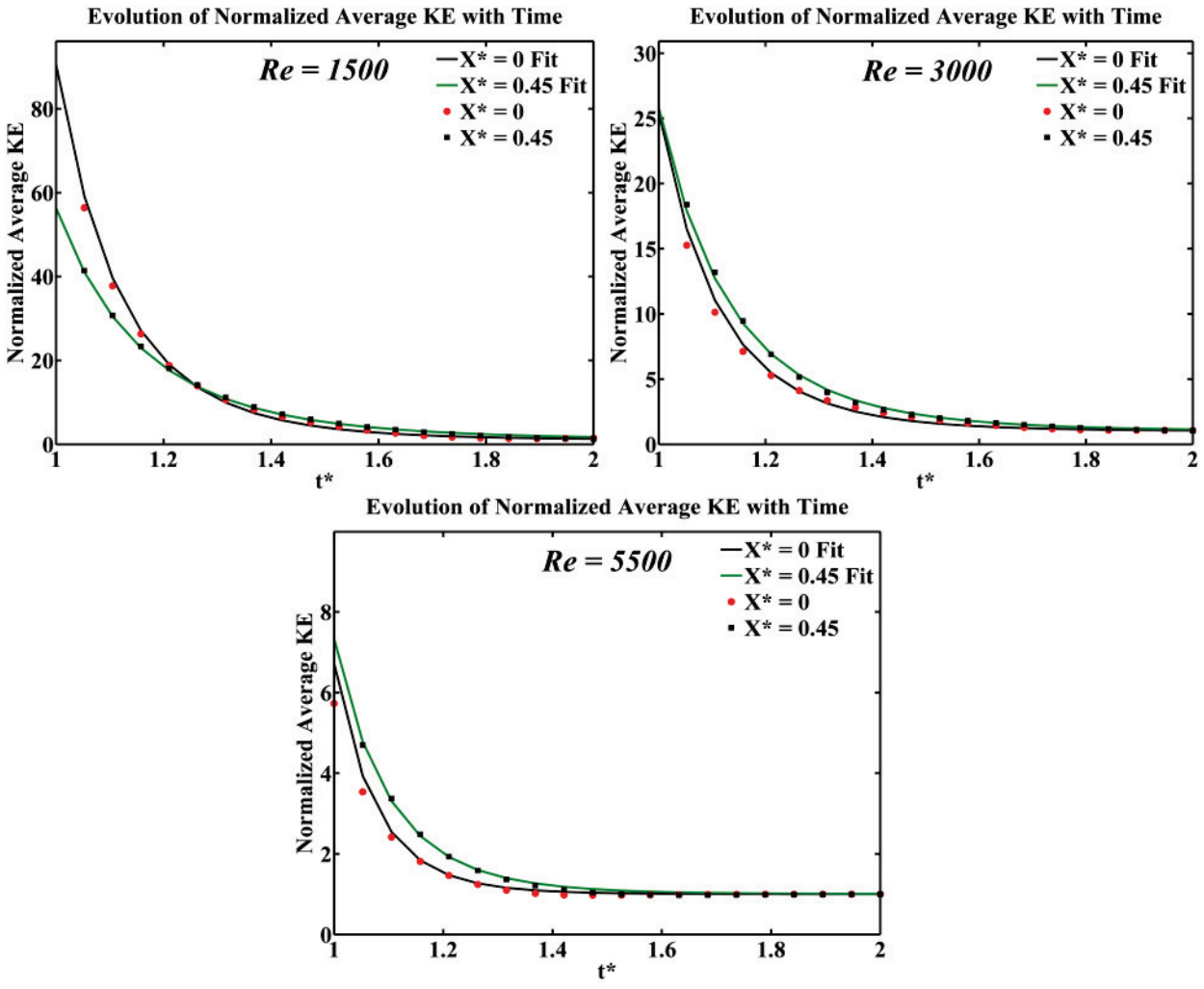

Figure 11 - Comparison of the decay of the normalized average kinetic energy at $x^* = 0$ and 0.45 with the power law fit for the three cases (Re = 1500, 3000, and 5500).

The Re = 1500 case experiences the largest growth in kinetic energy in comparison to its respective unforced case. For larger Reynolds numbers (lower Ψ), the growth is less since the flow has more inertia and therefore its motion is less affected by the impulsive body force. The temporal decay of kinetic energy is observed to be quicker for larger Reynolds numbers, for instance the time (Δt^*) required for the KE_{avg} at $x^* = 0.90$ to fall to 5% of its value from $t^* = 1$ was found to be 0.91, 0.66, and 0.46 in order of increasing Re. The temporal decay (from $t^* = 1$ onward) appears to follow a power law ($KE_{avg} \sim (t^*)^{-\alpha}$). To illustrate this point, figure 11 shows the agreement of the power law decay with the data for two sections downstream of the boundary

of the forced volume ($x^* = 0$ and $x^* = 0.45$). The exponent governing the rate of decay (α) increases for increasing Re (again indicating faster temporal decay for larger Re). In order of increasing Re, for $x^* = 0$ the exponents have values of 8.4, 8.9, and 13.1 whereas for $x^* = 0.45$ they have values of 6.3, 7.5, and 10.1. The spatial decay generally is quicker for lower Reynolds numbers. The distance (Δx^*) required for the KE_{avg} at $t^* = 0.53$ to fall to 5% of its value from $x^* = 0.90$ was 1.54, 1.95, and 2.32 again in order of increasing Re.

Figure 12 contains plots of normalized cross-sectionally averaged axial ($KE_x = 0.5U^2$) and in-plane ($KE_{yz} = 0.5V^2 + 0.5W^2$) kinetic energy at three selected sections ($x^* = 1.81$, 3.63, and 4.54) downstream of the forced volume. The kinetic energies were normalized with respect to the cross-sectionally averaged axial kinetic energy of the respective steady unforced case. The KE_x was subtracted by 1 to have the plots on the same scale. It can be seen that the peaks and troughs of the axial and in-plane kinetic energies often coincide, indicating a transfer of energy. In some instances, the secondary flow extracts kinetic energy from the mean flow however the reverse is seen to be more common. For example, in figure 12, for the section $x^* = 3.63$ of the $Re = 3000$ case, beginning at the end of the impact ($t^* = 1$), the KE_x increases while the KE_{yz} decreases by a similar magnitude. This is an indication that the secondary flow is dissipating energy into the mean flow.

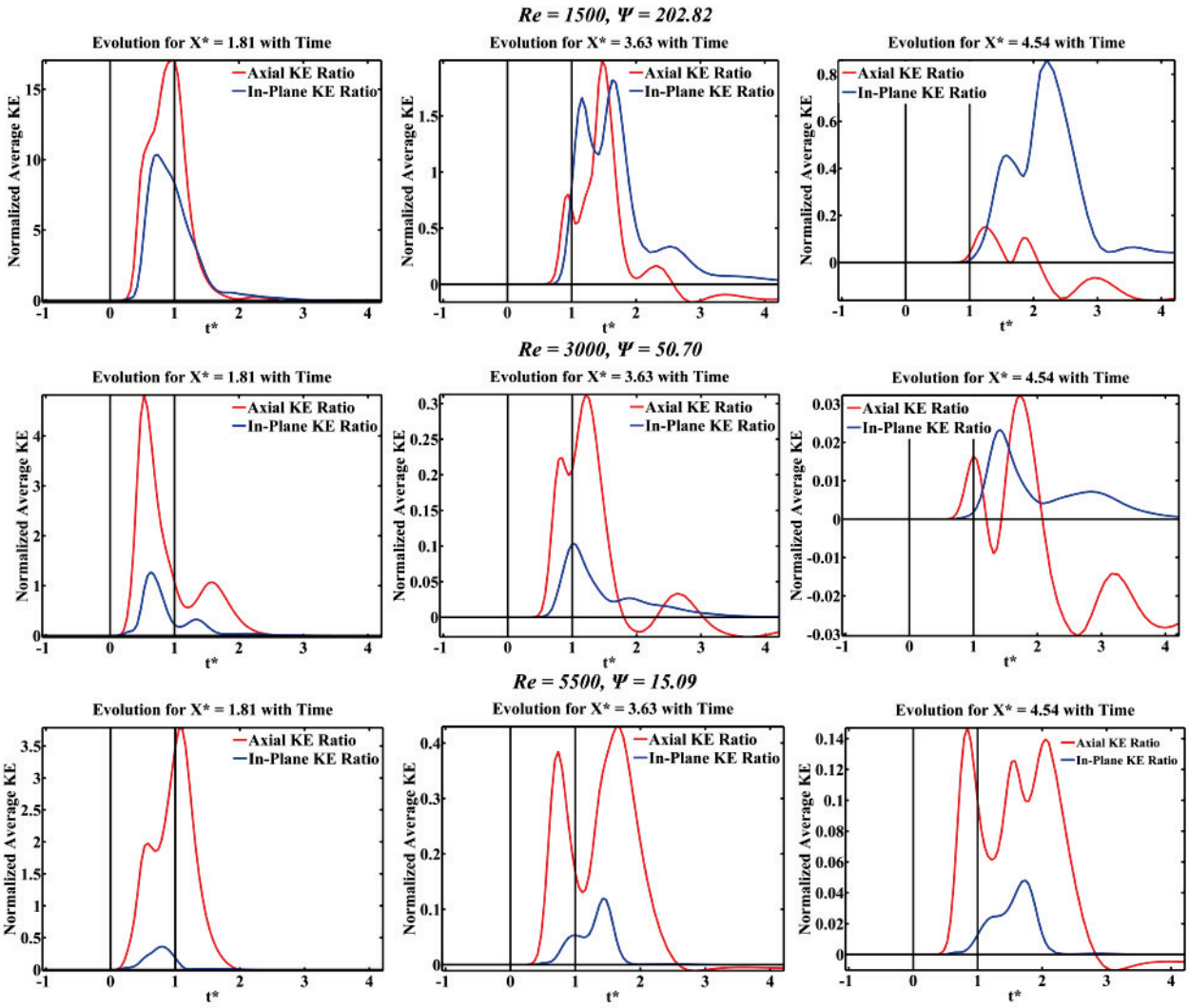

Figure 12 - Plots of axial and in-plane normalized average kinetic energies for Re = 1500, 3000, and 5500 at x^* = 1.81, 3.63, and 4.54. An alternating exchange in kinetic energy is observed between the axial and in-plane flows. This energy exchange corresponds to locations where a peak of one energy coincides with a trough of the other; for example, for Re = 3000 at x^* = 3.63 and t^* = 1, the secondary flow is dissipating energy into the mean flow.

Chapter 4 : Pulsatile Inlet Velocity

The impact was applied at three different instances during the pulsatile velocity profile, namely during the acceleration phase, the peak phase, and the deceleration phase. For an accelerating flow, there is a favorable streamwise pressure gradient. This pressure gradient adds to the transverse pressure gradient induced by the body force, resulting in a pressure gradient which is skewed counterclockwise in comparison with that in figure 6 (see figure 13). The opposite effect (the pressure gradient skewing in the clockwise direction with reference to figure 6) occurs when the body force is applied during the deceleration phase of the pulsatile profile.

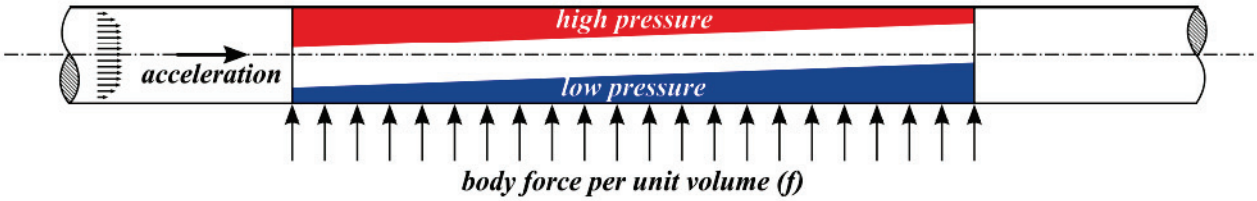

Figure 13 - Schematic of the skewed transverse pressure gradient induced by the action of the body force with the effects of fluid acceleration.

4.1 Velocity Field

At first glance, the axial and secondary flows exhibit similar features as for the uniform flow cases, particularly for an impact occurring during the peak phase (see figures 8 and 14). The induced pressure gradient results in the development of two streamwise vortices, in the same manner as discussed in section 3.1, which in turn results in secondary flows attempting to restore the equilibrium velocity profile. The axial velocity however, appears to respond more dramatically to the accelerating flow than the decelerating flow. This occurs due to the skewed pressure gradient, which is more pronounced for the impact occurring during the accelerating phase and less fluid is accelerated at the bottom of the pipe (the low pressure region is thinner at the upstream boundary of the forced volume). The development of the secondary flow also

appears to be slowest for an impact occurring during the accelerating phase and quickest for one occurring during the decelerating phase. These observations are in accordance with a study of ramp-type pipe flows by He & Jackson (2000). In their experimental work, a linearly increasing (and decreasing) flow rate is supplied through a circular pipe. They observed that the delay in radial turbulence propagation is larger for an accelerating flow than for a decelerating one. Since turbulent propagation occurs mainly by the diffusion of turbulent eddies, it is natural to expect a similar result for the secondary flows observed in this study.

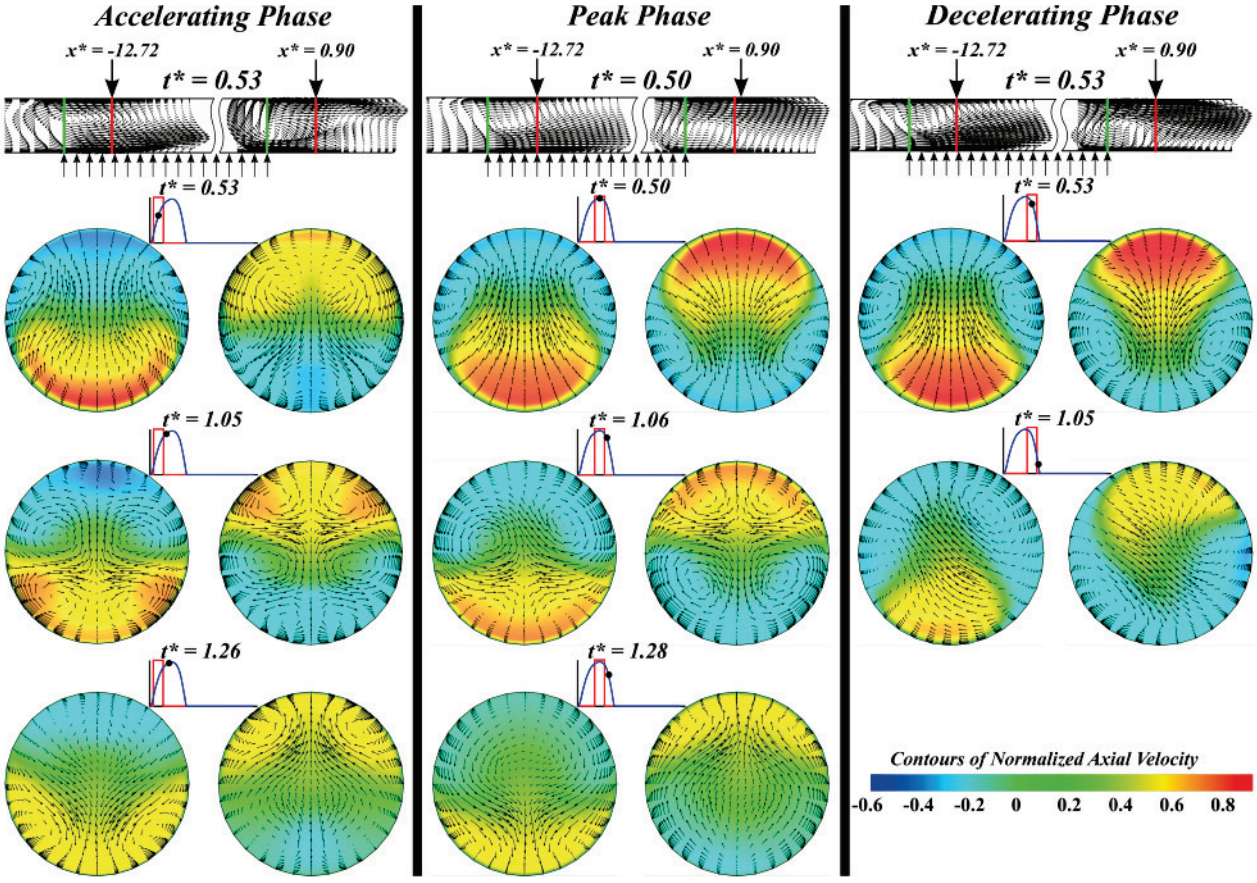

Figure 14 - Secondary flows and contours of normalized axial velocity at $t^* = 0.53$, 1.05, and 1.26 for the accelerating and decelerating phases and $t^* = 0.50$, 1.06, and 1.28 for the peak phase. Similar features as for the uniform flow cases are observed, however the time for the secondary flow to develop is longer from left to right (refer to the $t^* \approx 0.5$ sections).

4.2 Axial Skewness

Contours of axial skewness in the direction of the body force are plotted in figure 15. The

skewness is seen to be identically zero prior to the body force in all cases due to the symmetry of the axial velocity profile with respect to the $z = 0$ plane. When the body force is applied during the accelerating or peak phases of the pulsatile velocity profile, the skewness still attains a peak prior to the end of the impact. The degree of influence of the body force decreases for the accelerating flow whereas it is more or less constant for the impact occurring at the peak, which is why the peak skewness occurs earlier for the accelerating flow (at $t^* = 0.26$ for the accelerating phase compared to $t^* = 0.39$ for the peak phase). On the contrary, when the body force is applied during the decelerating phase, the peak skewness occurs precisely at the end of the impact ($t^* = 1$). This occurs because the degree of influence of the body force increases for a decelerating flow. In accordance with the degree of influence of the body force, the skewness peaks are 1.00, 0.63, and 1.38 for impacts occurring during the accelerating, peak, and decelerating phases respectively (all occurring at $x^* = 0.23$). At the top of the contour plots, the skewness is seen to grow after substantial decay, at least when the body force is applied during the accelerating and peak phases. This phenomenon occurs due to the presence of streamwise vortices in the flow which have not dissipated as quickly as the inlet velocity profile decayed to zero. These vortices result in some antisymmetry of the axial velocity profile with respect to the $z = 0$ plane and therefore, due to the definition of the axial skewness (equation 1), when the inlet velocity decays to zero the skewness may tend to a large number (which is seen to occur).

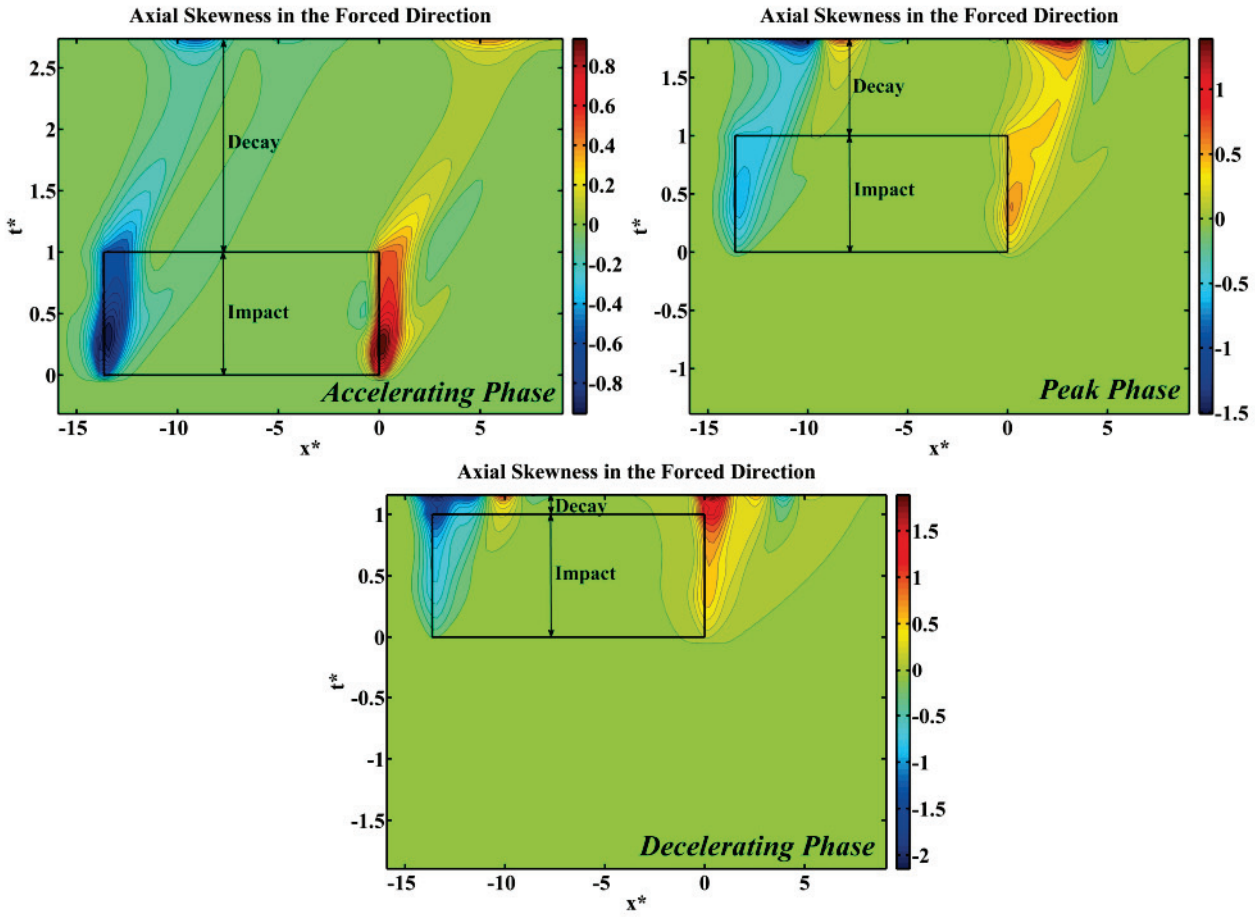

Figure 15 - Contours of axial skewness for an impact occurring during the accelerating, peak, and decelerating phases. The maximum skewness is largest for the decelerating phase and occurs at the end of the impact, whereas it occurs before the end of the impact for the accelerating and peak phases.

4.3 Kinetic Energy

Rather than investigating the ratio of the cross-sectionally averaged kinetic energy of the forced case with respect to the unforced case as in section 3.3, the difference per unit mass (Δke_{avg}) between the two was plotted in figure 16 (in order to avoid division by zero due to the base flow decaying to zero), which represents the increase in kinetic energy with reference to the base flow. The maximum observed kinetic energy increase for the three cases exhibit similar magnitudes. For instance, at the upstream boundary of the forced volume, the maximum Δke_{avg} is 3.30 m^2/s^2 (at $t^* = 0.37$ and $x^* = -13.41$), 3.28 m^2/s^2 (at $t^* = 0.44$ and $x^* = -13.41$), and 3.30 m^2/s^2

(at $t^* = 0.47$ and $x^* = -13.63$) for an impact occurring during the accelerating, peak, and decelerating phases respectively. At the downstream boundary, the maximum Δke_{avg} is, respectively, 3.12 m^2/s^2 (at $t^* = 0.32$ and $x^* = 0.23$), 3.28 m^2/s^2 (at $t^* = 0.39$ and $x^* = 0.23$), and 3.32 m^2/s^2 (at $t^* = 0.37$ and $x^* = 0$). Interestingly, at the upstream boundary, the maximum Δke_{avg} occurs at successively later times between each case, again in accordance with the concept of the degree of influence. At the downstream boundary however, this is not the case. More interestingly, for the accelerating phase, the peak Δke_{avg} downstream occurs at a later time than the peak in skewness ($t^* = 0.32$ compared to $t^* = 0.26$). The reverse occurs for the decelerating flow, however this is expected since the flow itself decays to zero and the Δke_{avg} must, of course, attain a maximum before then. The effects of the body force are still seen to be localized at the boundaries of the forced volume for all cases, however the evolution of kinetic energy is clearly different depending on the nature of the flow. For the accelerating flow, the Δke_{avg} contours appear more localized spatially and elongated temporally. The opposite is seen for the decelerating flow, where the contours are wider spatially and more localized temporally. For the impact occurring during the peak phase, the inlet velocity is more or less constant and the result appears similar to the normalized average kinetic energy for the $Re = 5500$ case in figure 8. Figure 16 also shows the evolution of the Δke_{avg} from the upstream boundary of the forced volume (for $x^* = -13.63$, -13.18, -12.72, -12.27, -11.81, -11.36, and -6.81) to illustrate the spatial and temporal decay just discussed. Note that for $x^* = -6.81$ (the middle of the forced volume), $\Delta ke_{avg} \approx 0$.

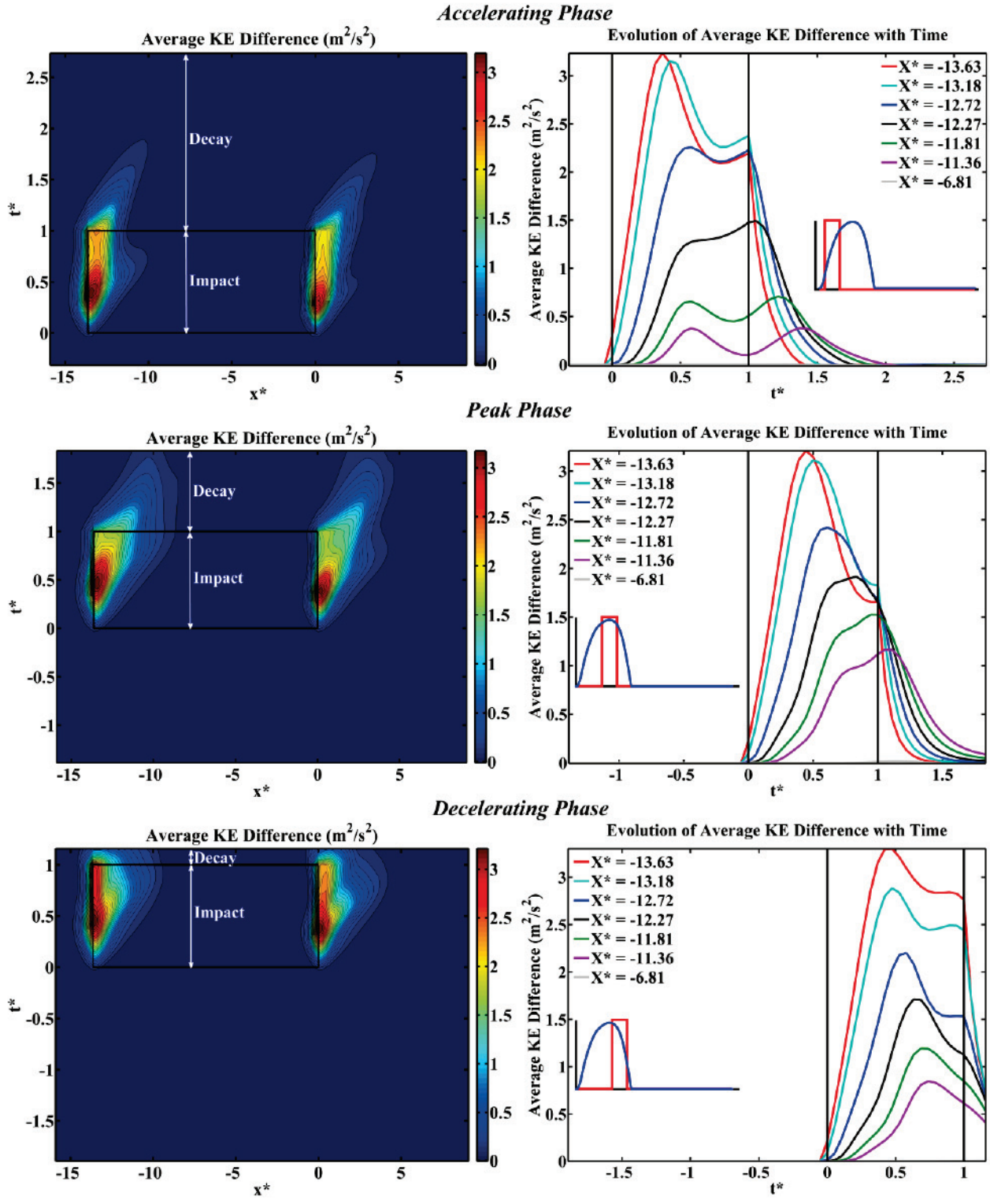

Figure 16 - Contours of average kinetic energy difference for an impact occurring during the accelerating, peak, and decelerating phases and plots at different upstream sections along the pipe. The kinetic energy is more localized spatially and elongated temporally for the accelerating flow whereas the opposite is seen for the decelerating flow.

The temporal decay of the kinetic energy also follows a power law ($\Delta ke_{avg} \sim (t^*)^{-\alpha}$) for the pulsatile cases as for the uniform flow cases. Figure 17 shows the agreement of the power law fit with the decay only for the accelerating and peak phases for two sections upstream (x^* = -13.63 and -12.27) since the kinetic energy did not completely decay for the decelerating phase by the end of the simulation. For x^* = -13.63 and -12.27, the decay rates (α) are respectively 10.8 and 5.0 for the accelerating phase and 12.3 and 5.6 for the peak phase. From the decay rate, it can be seen that the temporal decay is longest for the accelerating phase. From figure 16, it appears as though the temporal decay would be shortest for the decelerating phase, however further study would be required. It is interesting to note that such a power law decay has been experimentally observed for the turbulent kinetic energy for decaying homogeneous and isotropic turbulence (Townsend 1976, Wilcox 1994). It would be expected therefore, that such a decay may be a feature of using a turbulence model, since the decay of the kinetic energy of the mean flow and the decay of the turbulent kinetic energy are correlated (i.e. as the mean flow decays, so should the turbulent fluctuations since there will not be enough energy to sustain them). The fact that the Re = 1500 case (see figure 11) also decays as a power law suggests that this result is not an artifact of the turbulence model.

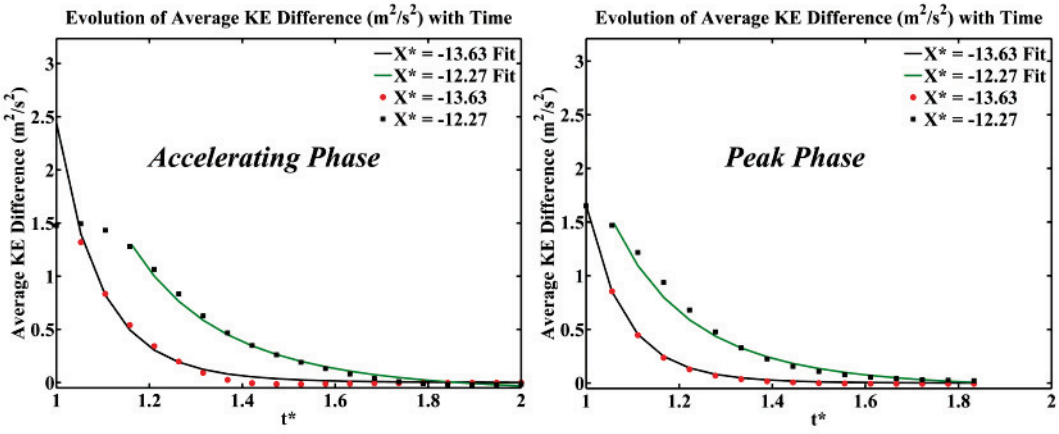

Figure 17 - Comparison of the decay of the average kinetic energy difference at x^* = -13.63 and -12.72 with the power law fit for an impact occurring during the accelerating and peak phases.

Chapter 5: Conclusions & Recommendations

5.1 Summary

In this fundamental study, the effects of a localized transverse impulsive body force on circular pipe flow was investigated for two flow conditions through numerical simulation. A parameter, Ψ, was also devised that quantifies the degree of influence of the body force by measuring the ratio of the induced transverse pressure gradient to the streamwise pressure gradient.

For the first flow condition, three different constant inlet velocities were tested, namely with Reynolds numbers of 1500, 3000, and 5500. At the moment the body force was applied, a transverse pressure gradient equal in magnitude and opposite in direction of the body force develops in the forced section of the pipe. This pressure gradient results in two zones of adverse pressure gradient from which two counter-rotating streamwise vortices develop. Secondary flows develop in conjunction with these streamwise vortices, acting in a manner so as to restore the equilibrium velocity profile by carrying fluid from high axial velocity regions, through the boundary layer, and back to the mean flow. The effects of the body force are localized at the boundaries of the forced volume and the lower the Reynolds number, the more localized the effects are and the more the velocity field is skewed. Maximum skewing of the velocity profile occurred during the impact rather than at the end, with larger skewing occurring for higher Ψ. The temporal decay of kinetic energy was observed to be faster for larger Reynolds numbers and is governed by a power law decay, whereas the spatial decay was faster for lower Reynolds numbers (since the effects propagate downstream at a slower speed). An alternating exchange in energy between the axial and secondary flows was also observed.

For the second flow condition, a pulsatile inlet velocity was used corresponding to the

systolic duration of the cardiac cycle. The effects of the impulsive body force was investigated by applying the force at three different instances of the pulsatile profile, namely during the accelerating, peak, and decelerating phases. Application of the force during the accelerating phase resulted in a pressure gradient skewed counterclockwise with regard to the constant inlet velocity cases. The opposite effect occurred when the force was applied during the decelerating phase. The streamwise vortices and secondary flows develop and act, generally, in the same manner as for the constant inlet velocity cases. It was observed, however, that the development of the secondary flow occurs later for the accelerating flow case and fastest for the decelerating flow. The maximum skewing of the axial velocity profile was largest for the decelerating phase occurring at the end of the impact, whereas it occurred before the end of the impact for the accelerating and peak phases. The maximum skewing occurred at successively later times for the accelerating, peak, and decelerating phases respectively. This can be understood in terms of the degree of influence which decreases for an accelerating flow and increases for a decelerating flow. The kinetic energy exhibited a shorter spatial decay for the accelerating phase than for the decelerating phase (the longest spatial decay actually occurs for the peak phase). The temporal decay of kinetic energy also appears to follow a power law decay and was observed be longer for the accelerating phase than for the peak phase.

5.2 Limitations and Future Directions

The main limitation of this study was the choice of using a turbulence model. An improved study would require the use of direct numerical simulation (DNS) as no assumptions are made regarding the nature of the flow and the governing equations are solved exactly. Another limitation of the study is that the results should be compared with some experimental data. Notably, from the problem definition, it is not trivial to perform an experiment for this study,

however there are ways in which it can be achieved. Using a magnetorheological fluid, application of a strong impulsive transverse magnetic field on a localized section of a long circular pipe may be a sufficient experimental apparatus, however it may be difficult to measure the velocity field in this case.

As a future direction for study, a numerical simulation of such an impulsive body force acting on a realistic model of an aorta should be conducted, and the concepts observed here may be used to understand the more complex flow. It would also be interesting to investigate the effects of the body force on pure ramp-type inlet flows in a circular pipe to gain a deeper understanding of the observed phenomena in the pulsatile cases by varying the ramp rate and the start and end velocities (as done be He & Jackson 2000). Also, rather than only investigating different inlet flows, it would also be interesting to study the effects of the magnitude and duration of the body force as well as different types of forcing functions.

References

ANSYS Inc. "ANSYS FLUENT 12.0 Theory Guide." April 2009.

Berger SA, Talbot L, Yao LS. "Flow in curved pipes." Annual Reviews of Fluid Mechanics. 15: 461-512. 1983.

Boiron O, Deplano V, Pelissier R. "Experimental and numerical studies on the starting effect on the secondary flow in a bend." Journal of Fluid Mechanics. 574: 109-29. 2007.

Celik IB. "Procedure for estimation and reporting of uncertainty due to discretization in CFD applications." Journal of Fluids Engineering. 130 (7): 1-4. 2008.

Chandratilleke TT, Nadim N. "Forced convective heat transfer and fluid flow characteristics in curved ducts." An Overview of Heat Transfer Phenomena. Rijeka, Croatia: InTech. 125-50. 2012.

Chapman SJ, et al. "Blunt traumatic aortic injury." Nottingham, UK: UK Mathematics in Medicine Study Group. 2001.

Chiesa R, et al. "Traumatic rupture of the thoracic aorta." Acta Chirurgica Belgica. 103 (4): 364-74. 2003.

Dean WR. "Note on the motion of fluid in a curved pipe." The London, Edinburgh, and Dublin Philosophical Magazine and Journal of Science: Series 7. 4 (20): 208-23. 1927.

Dean WR. "The stream-line motion of fluid in a curved pipe." The London, Edinburgh, and Dublin Philosophical Magazine and Journal of Science: Series 7. 5 (30): 673-95. 1928.

Eckhardt B, et al. "Turbulence transition in pipe flow." Annual Reviews of Fluid Mechanics. 39: 447-68. 2007.

Eustice J. "Flow of water in curved pipes." Proceedings of the Royal Society of London: Series A. 84 (568): 107-18. 1910.

Eustice J. "Experiments on stream-line motion in curved pipes." Proceedings of the Royal Society of London: Series A. 85 (576): 119-31. 1911.

Ghalichi F, et al. "Low Reynolds number turbulence modeling of blood flow in arterial stenosis." Biorheology. 35 (4-5): 281-94. 1998.

Griffith MD, et al. "Effect of small asymmetries on axisymmetric stenotic flow." Journal of Fluid Mechanics (Rapids). 721: 1-11. 2013.

He S, Jackson JD. "A study of turbulence under conditions of transient flow in a pipe." Journal of Fluid Mechanics. 408: 1-38. 2000.

Kerswell RR. "Recent progress in understanding the transition to turbulence in a pipe." Nonlinearity. 18: 17-44. 2005.

Keshavarz-Motamed Z, Kadem L. "3D pulsatile flow in a curved tube with coexisting model of aortic stenosis and coarctation of the aorta." Medical Engineering & Physics. 33 (3): 315-24. 2011.

Keshavarz-Motamed Z, Garcia J, Kadem L. "Fluid dynamics of coarctation of the aorta and effect of bicuspid aortic valve." Plos One. 8 (8): e72394. 2013.

Launder BE, Sharma BI. "Application of the energy-dissipation model of turbulence to the calculation of flow near a spinning disc." Letters in Heat and Mass Transfer. 1: 131-8. 1974.

LeVeque RJ. "Finite Volume Methods for Hyperbolic Problems." Cambridge, UK: Cambridge University Press. 2002.

McConalogue DJ, Srivastava RS. "Motion of fluid in a curved tube." Proceedings of the Royal Society of London: Series A. 307: 37-53. 1968.

Menter FR. "Zonal two-equation k-ω turbulence models for aerodynamics flows." 24th Fluid Dynamics Conference. AIAA 93-2906: 1-21. 1993.

Menter FR, Kuntz M, Langtry R. "Ten years of industrial experience with the SST turbulence model." Turbulence, Heat and Mass Transfer. 4: 625-32. 2003a.

Menter FR, et al. "The SST turbulence model with improved wall treatment for heat transfer predictions in gas turbines." Proceedings of the International Gas Turbine Congress. IGTC2003-TS-059: 1-7. 2003b.

Menter FR, et al. "A correlation-based transition model using local variables - Part I: model formulation." Journal of Turbomachinery. 128 (3): 413-22. 2006.

Menter FR. "Review of the shear-stress transport turbulence model experience from an industrial perspective." International Journal of Computational Fluid Dynamics. 23 (4): 305-16. 2009.

Munson BR, et al. "Fundamentals of Fluid Mechanics." Hoboken, USA: John Wiley & Sons Inc. 2013.

Ottesen JT, Olufsen MS, Larsen JK. "Applied Mathematical Models in Human Physiology." Philadelphia, USA: SIAM. 2004.

Pezzella AT, Polimenakos AC. "Blunt thoracic aortic injury (BTAI): advances in the era of innovation, a review (Part I)." Annales de chirurgie thoracique et cardio-vasculaire. 3 (2): 50-65. 2008.

Rout SK, et al. "Numerical analysis of mixed convection through an internally finned tube." Cairo, Egypt: Hindawi Publishing Corporation. 2012.

Ryval J, Straatman AG, Steinman DA. "Two-equation turbulence modeling of pulsatile flow in a stenosed tube." Journal of Biomedical Engineering. 126: 625-35. 2004.

Salwen H, Cotton FW, Grosch CE. "Linear stability of Poiseuille flow in a circular pipe." Journal of Fluid Mechanics. 23: 601-39. 1980.

Lee SH. "A three-dimensional computational analysis of blood flow and fluid-structure interactions in the human aorta during traumatic rupture conditions." Charlottesville, USA: PhD Dissertation, University of Virginia. 2008.

Schilt S, et al. "The effects of time-varying curvature on velocity profiles in a model of the coronary arteries. Journal of Biomechanics. 29 (4): 469-74. 1996.

Siggers JH, Waters SL. "Steady flows in pipes with finite curvature." Physics of Fluids. 17 (077102): 1-18. 2005.

Thomson J. "On the origin of windings of rivers in alluvial plains, with remarks on the flow of water round bends in pipes." Proceedings of the Royal Society of London. 25: 5-8. 1876.

Tillack MS, Morley NB. "Magnetohydrodynamics." Standard Handbook for Electrical Engineers, 14th Edition. New York City, USA: McGraw-Hill. 1998.

Townsend AA. "The Structure of Turbulent Shear Flow." 2nd Edition. Cambridge, UK: Cambridge University Press. 1976.

Verkaik AC. "Analysis of velocity profiles in curved tubes." Eindhoven, Netherlands: PhD Dissertation, Eindhoven University of Technology. 2008.

Versteeg HK, Malalasekera W. "An Introduction to Computational Fluid Dynamics: The Finite Volume Method." Essex, England: Pearson Education Limited. 2007.

Wilcox DC. "Reassessment of the scale-determining equation for advanced turbulence models." AIAA Journal. 26 (11): 1299-310. 1988.

Wilcox DC. "Turbulence Modeling for CFD." La Cañada, USA: DCW Industries Inc. 1994.

Appendix

User-Defined Function for Body Force

The following code is written in the programming language C. The times t_1 and t_2 were changed for each case according to that defined in the problem definition (section 2.1).

```
#include "udf.h"

#define fmax 500000.0
#define t1 0.1
#define t2 0.2

/* sterm: The name of this UDF. */
/* C: The cell. */
/* T: The thread. */
/* dS: The derivative of the source term with respect to the variable eqn. */

/* Note: For momentum source terms, eqn refers to the velocity component in the
direction specified in FLUENT. */

DEFINE_SOURCE(sterm, C, T, dS, eqn)
{
    real f;

    real t = CURRENT_TIME;

    if (t >= t1 && t <= t2)
    {
        f = fmax;
    }
    else
        f = 0.0;

    dS[eqn] = 0.0;

    return f;
}
```